Metal-ion rescue revisited: Biochemical detection of site-bound metal ions important for RNA folding

JOHN K. FREDERIKSEN,[1,2,5] NAN-SHENG LI,[2,3] RHIJU DAS,[4,6] DANIEL HERSCHLAG,[4,6] and JOSEPH A. PICCIRILLI[2,3,6]

[1]The Pritzker School of Medicine, [2]Department of Biochemistry and Molecular Biology, [3]Department of Chemistry, The University of Chicago, Chicago, Illinois 60637, USA
[4]Department of Biochemistry, Beckman Center, Stanford University, Stanford, California 94305-5307, USA

ABSTRACT

Within the three-dimensional architectures of RNA molecules, divalent metal ions populate specific locations, shedding their water molecules to form chelates. These interactions help the RNA adopt and maintain specific conformations and frequently make essential contributions to function. Defining the locations of these site-bound metal ions remains challenging despite the growing database of RNA structures. Metal-ion rescue experiments have provided a powerful approach to identify and distinguish catalytic metal ions within RNA active sites, but the ability of such experiments to identify metal ions that contribute to tertiary structure acquisition and structural stability is less developed and has been challenged. Herein, we use the well-defined P4–P6 RNA domain of the *Tetrahymena* group I intron to reevaluate prior evidence against the discriminatory power of metal-ion rescue experiments and to advance thermodynamic descriptions necessary for interpreting these experiments. The approach successfully identifies ligands within the RNA that occupy the inner coordination sphere of divalent metal ions and distinguishes them from ligands that occupy the outer coordination sphere. Our results underscore the importance of obtaining complete folding isotherms and establishing and evaluating thermodynamic models in order to draw conclusions from metal-ion rescue experiments. These results establish metal-ion rescue as a rigorous tool for identifying and dissecting energetically important metal-ion interactions in RNAs that are noncatalytic but critical for RNA tertiary structure.

Keywords: diffuse ion atmosphere; metal-ion rescue; phosphorothioate; RNA; RNA structure and folding

INTRODUCTION

When RNA molecules adopt compact three-dimensional architectures, the negative charge of the ribose-phosphate backbone generates enormous repulsive energy. Counteracting this repulsion, cations condense onto all RNA molecules, forming a counterion atmosphere (Manning 1977a, 1978; Bukhman and Draper 1997; Misra and Draper 1998; Das et al. 2005b; Draper et al. 2005; Chu et al. 2008; Leipply et al. 2009). While the vast majority of cations associated with RNA reside in this diffuse ion atmosphere, some ions associate more intimately with the RNA, using their hydration shells to bind to specific sites via hydrogen bonding (outer-sphere coordination) or shedding water molecules to coordinate directly to an RNA heteroatom (inner-sphere coordination). These site-bound metal ions often appear in intricate structures within folded RNAs and, in the case of several ribozymes, participate directly in catalysis (Chen et al. 1997; Sontheimer et al. 1997; Shan et al. 1999; Gordon et al. 2007). Accordingly, understanding RNA structure and function requires knowing the locations of site-bound metal ions and the thermodynamics of their interactions with RNA.

Metal-ion rescue experiments, first used to delineate metal-ion substrate interactions in protein enzyme active sites (Jaffe and Cohn 1978; Darby and Trayer 1983; Lee and O'Sullivan 1985; Pecoraro et al. 1985), have been expanded in ribozyme studies to provide a powerful strategy to identify individual metal ions, define their ligands, and assign their roles in catalysis (Piccirilli et al. 1993; Chen et al. 1997; Sontheimer et al. 1997; Weinstein et al. 1997; Shan et al. 1999; Yoshida et al. 1999; Hougland et al. 2005; Gordon

[5]**Present address:** Department of Pathology and Laboratory Medicine, The University of Rochester Medical Center, Rochester, NY 14642, USA.
[6]**Corresponding authors.**
E-mail jpicciri@uchicago.edu.
E-mail herschla@stanford.edu.
E-mail rhiju@stanford.edu.
Article published online ahead of print. Article and publication date are at http://www.rnajournal.org/cgi/doi/10.1261/rna.028738.111.

et al. 2007; Forconi et al. 2008; Forconi and Herschlag 2009). The rescue approach relies on the differential preferences of Mg^{2+} and "softer" divalent metal ions like Mn^{2+}, Cd^{2+}, and Zn^{2+} to coordinate oxygen vs. sulfur or nitrogen ligands. As Mg^{2+} coordinates these ligands more weakly than it coordinates oxygen, sulfur or nitrogen substitution of an oxygen ligand can disrupt the Mg^{2+} interaction, leading to deleterious effects on activity. Inclusion of cations that interact more strongly than Mg^{2+} with sulfur or nitrogen often restores the disrupted interaction, resulting in suppression of the deleterious effect, or "rescue." In practice, these experiments require quantitative analysis of the energetic effects of the substitution in the presence of Mg^{2+} and in the presence of the rescuing cation M^{2+} to provide the most reliable and extensive information about the number of bound metal ions and their interactions (Shan et al. 1999; Wang et al. 1999; Christian 2005; Forconi and Herschlag 2009).

In principle, this metal-ion rescue approach should also be a powerful biochemical tool for identifying metal-ion sites important for folding and conformational transitions in structured and signaling RNA molecules. However, a previous study of sulfur interferences in the independently folding P4–P6 RNA domain did not correspond well with structural data (Basu and Strobel 1999). Using a nondenaturing gel electrophoresis assay that probes the fraction of folded RNA by the differential migration of compact and extended forms, a population of P4–P6 RNAs containing a random distribution of R_P-phosphorothioates was screened to identify sites within the domain where R_P-phosphorothioate substitution interferes with global compaction (Cate et al. 1997; Basu and Strobel 1999). The identified sites included a subset of the ligands for metal ions observed crystallographically. Within this subset, Mn^{2+} and other soft metal ions suppressed phosphorothioate interference of global compaction at some, but not all, inner-sphere ligands (Basu and Strobel 1999). In addition, Mn^{2+} apparently suppressed phosphorothioate interference of folding by two outer-sphere ligands, a result that called into question the usual inference that metal-ion rescue reveals sites of inner-sphere coordination (Basu and Strobel 1999).

The apparent outer-sphere rescue could have major implications for published and future studies applying metal-ion rescue approaches to both RNA catalysis and RNA conformational transitions. Consequently, we sought to determine whether these results in the P4–P6 RNA identified a fundamental limitation of metal-ion rescue or a limitation of the study's methodology and analysis. Addressing these issues successfully could establish proof-of-concept for adapting the rescue approach to the investigation of metal ions in nonenzymatic, noncoding RNAs (ncRNAs), which likely encompass the vast majority of metal-ion binding sites within the cellular RNAome (Costa 2010).

We have synthesized variants of P4–P6 RNA bearing phosphorothioate modifications at specific locations and used hydroxyl radical footprinting to characterize the Mg^{2+}- and Mn^{2+}-induced folding transitions of these variants. Rescue is observed at positions identified as inner sphere in the P4–P6 crystal structures, but not at outer-sphere positions. These results clarify limitations of prior metal-ion rescue experiments and provide strong support for the power of the approach for investigating RNA folding and conformational changes, as well as a rigorous template for carrying out such studies.

RESULTS AND DISCUSSION

The "standard" thermodynamic framework for RNA folding and metal-ion rescue

For metal-ion rescue and other experiments that probe interactions, one would ideally make direct comparisons of free energies via thermodynamic cycles. A thermodynamic cycle for folding of unmodified and thio-modified P4–P6 (O and S, respectively) in the presence of Mg^{2+} or Mn^{2+} is shown in Scheme 1A, and the folding free energies are compared via the $\Delta\Delta G$ values defined in Scheme 1B. Rescue would correspond to the observation of amelioration of a folding defect—an increase in ΔG_{fold} (less favorable folding) for folding of the thio-substituted RNA in Mg^{2+} that is alleviated in the presence of a softer metal ion such as Mn^{2+} (Scheme 1B). In terms of the free energies defined in Scheme 1B, if folding is affected similarly in Mg^{2+} and Mn^{2+}, no rescue occurs ($\Delta\Delta\Delta G_{rescue} = 0$), whereas a positive value of $\Delta\Delta\Delta G_{rescue}$ would indicate rescue.

Evaluating metal-ion rescue quantitatively therefore requires estimating free energies of folding. RNA folding is typically followed as a function of metal-ion concentration, with different RNAs exhibiting different folding transitions. For each RNA, the experimentally observed "fraction folded" is typically fit to the Hill model:

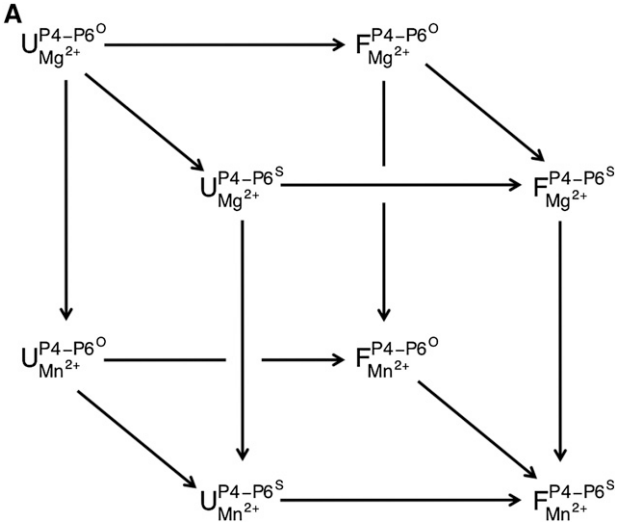

SCHEME 1A.

B

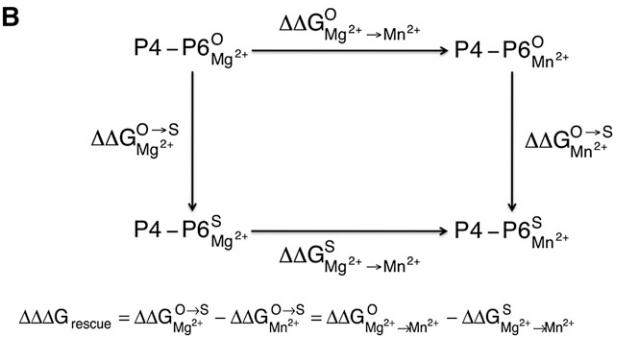

SCHEME 1B.

$$\text{Fraction folded} = \frac{\left(\frac{[M^{2+}]}{[M^{2+}]_{1/2}}\right)^{n}}{1+\left(\frac{[M^{2+}]}{[M^{2+}]_{1/2}}\right)^{n}}. \quad (1)$$

Here, $[M^{2+}]$ is the metal-ion concentration, and $[M^{2+}]_{1/2}$ and n are the transition midpoint and apparent Hill coefficient, respectively (Fang et al. 1999; Rook et al. 1999; Das et al. 2005b). This model corresponds to a free-energy difference between the unfolded and folded state of

$$\Delta G = -nRT\ln\left(\frac{[M^{2+}]}{[M^{2+}]_{1/2}}\right), \quad (2)$$

where R is the gas constant and T is the temperature. Values for "fraction folded" are readily determined for $[M^{2+}]$ around the transition midpoints' $[M^{2+}]_{1/2}$ values, but extrapolation of inferred folding free energies to higher and lower metal-ion concentrations is necessary to compare RNA variants with different stabilities. If the apparent Hill coefficient n remains constant between unmodified and thio-modified variants, the free-energy difference is directly related to the ratio of the folding midpoints $[M^{2+}]^{O}_{1/2}$ and $[M^{2+}]^{S}_{1/2}$:

$$\Delta\Delta G = -nRT\ln\left(\frac{[M^{2+}]^{O}_{1/2}}{[M^{2+}]^{S}_{1/2}}\right). \quad (3)$$

If folding of both the unmodified and thio-modified RNAs is measured in Mg^{2+} and Mn^{2+}, and titrations in both metal ions happen to again yield the same Hill coefficient n, this framework gives

$$\Delta\Delta\Delta G = -nRT\ln\left[\frac{\left(\frac{[M^{2+}]^{O}_{1/2}}{[M^{2+}]^{S}_{1/2}}\right)_{Mg^{2+}}}{\left(\frac{[M^{2+}]^{O}_{1/2}}{[M^{2+}]^{S}_{1/2}}\right)_{Mn^{2+}}}\right]. \quad (4)$$

In this scenario, describing the metal-ion rescue results in terms of "fold rescue" is equivalent to discussing the free-energy differences $\Delta\Delta\Delta G$, with a quantitative translation provided by Equation 4. Nevertheless, as discussed further below, two problems frequently complicate this description. First, fitted Hill coefficients often differ for destabilized variants or when different metal ions induce folding. Equations 3 and 4 are not applicable in these situations, and Equation 2 leads to free-energy estimates that depend on the choice of reference metal-ion concentration. Second, distinct, partially folded states are frequently observed at intermediate M^{2+} concentrations (see below, "Low salt comparisons"), so that a single midpoint and Hill coefficient are not sufficient to describe a folding titration. Instead, multiple folding transitions must be interrogated and characterized.

One approach for minimizing these problems and simplifying analyses is to saturate the ion atmosphere with a high concentration of monovalent cations, such that any associated divalent cations occupy specific metal-ion binding sites nearly exclusively, rather than the ion atmosphere (Bukhman and Draper 1997; Horton et al. 1998). This approach has been directly tested and validated with P4–P6 RNA, where structure mapping and direct ion counting assays showed a congruence of simple two-state folding with a Hill slope of 2 and binding of two Mg^{2+} ions (Scheme 2; Das et al. 2005b). We therefore first investigated P4–P6 folding and metal-ion rescue in a background of 2 M NaCl. We then turned to more standard conditions of low monovalent salt concentration, such as were used in the prior metal-ion rescue study (Basu and Strobel 1999). We first present results in terms of "fold rescue," qualitatively comparing effects for substitution of inner- and outer-sphere ligands. To take into account observations of varying Hill coefficients (and later, additional intermediates), we developed general thermodynamic treatments that allow systematic estimation of free-energy differences for metal-ion-dependent folding events, and provide quantitative support for the specific conclusions herein.

Mg^{2+}- and Mn^{2+}-induced folding of P4–P6 in 2 M NaCl

The P4–P6 domain (Murphy and Cech 1993) consists of two sets of coaxially stacked helices—P4–P5–P6 and P5a–P5b—joined by a hinge region (J5/5a) (Fig. 1A,B). Two interactions connect these helical stacks in the folded state: a tetraloop-receptor interaction between the loop of P5b and internal loops in P6 (J6a/b and J6b/a) and an A-minor interaction between an A-rich bulge within P5a and the P4

$$I_{TL-TR} + 2M^{2+} \rightleftharpoons F \bullet 2M^{2+}$$

SCHEME 2.

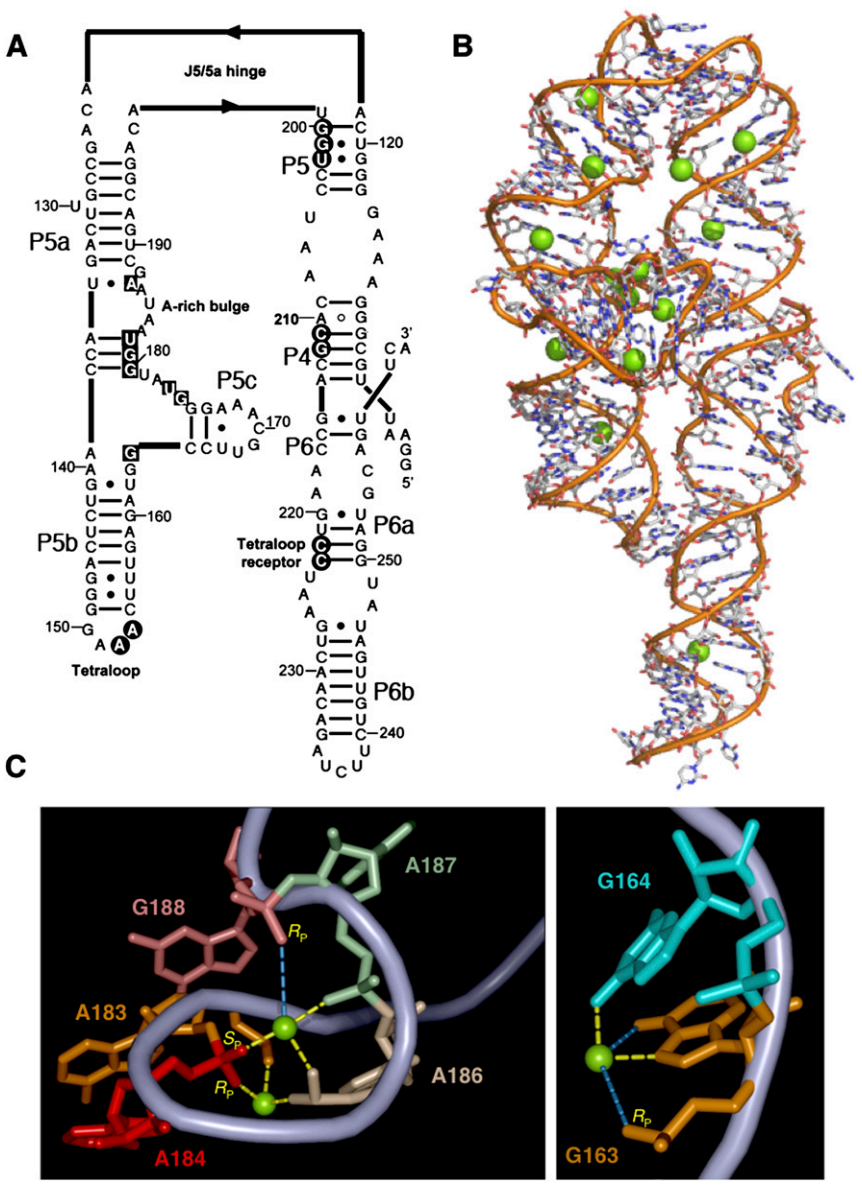

FIGURE 1. Structure of ΔC209 P4–P6 RNA. (*A*) Secondary structure of ΔC209 P4–P6. Nucleotides protected from hydroxyl radical cleavage in the folded state are shown as black circles (tertiary protections) or as black squares (subdomain protections). (*B*) Crystal structure of ΔC209 P4–P6 (derived from PDB file 1HR2). Green spheres represent magnesium ions observed in the structure. (*C*) Detail of metal ion binding sites in ΔC209 P4–P6 relevant to this work. Within the A-rich bulge (*left*) and the trihelical junction (*right*), magnesium ions make several inner-sphere (yellow dashes) and outer-sphere (blue dashes) contacts to nucleobases and nonbridging phosphate oxygens. The specific phosphate oxygens modified in this work are labeled in yellow text.

helix. We refer to these connections as "tertiary interactions" herein. In our studies we have used ΔC209 P4–P6 RNA. The deletion of C209 thermostabilizes the folded RNA; the normally extruded A210 forms a noncanonical base pair with G111 within the P4 helix (Juneau and Cech 1999), but the structure is otherwise unchanged from wild-type P4–P6 (Juneau et al. 2001). We refer to this construct as P4–P6 or unmodified P4–P6 throughout for simplicity, unless noted otherwise.

Several Mg^{2+} ions are observed in the crystal structures of P4–P6 (Cate et al. 1996; Juneau et al. 2001). Within the A-rich bulge, two Mg^{2+} ions each make three inner-sphere contacts to nonbridging phosphate oxygen atoms contributed by A183, A184, A186, and A187 (Fig. 1C, left). In addition, the *pro-*R_P nonbridging oxygen of G188 lies within outer-sphere coordination distance of one of these metal ions. A third metal ion directly coordinates the N7 and O6 atoms of G163 and G164, respectively, and makes an apparent outer-sphere contact to the *pro-*R_P nonbridging oxygen of G163 (Fig. 1C, right). These metal ions bind within the P5abc subdomain, which can undergo divalent metal-ion-dependent folding in isolation (Murphy and Cech 1993; Wu and Tinoco 1998; Silverman et al. 1999; Zheng et al. 2001). Several other metal ions are observed in P4–P6 crystal structures, but are not addressed herein.

In 2 M NaCl, wild type P4–P6 acquires nearly all native long-range tertiary contacts (Takamoto et al. 2004; Das et al. 2005b). The remaining tertiary interactions—those within P5abc and between the A-rich bulge (residues 182–188) and the P4 helix—are in the vicinity of the inner-sphere metal ions and form only upon addition of divalent metal ions (Fig. 2). Initial experiments showed that ΔC209 P4–P6 forms the same tertiary interactions in 2 M NaCl, as reflected by protection from hydroxyl radical cleavage of nucleotides 152–153 (P5b tetraloop), 200–202 (J5/5a hinge), and 222–223 (tetraloop-receptor) (Fig. 1A; data not shown). This state is termed $I_{TL\text{-}TR}$ herein. The addition of Mg^{2+} or Mn^{2+} induces protection of P5abc subdomain nucleotides 164, 176–177, 180–182, and 187, as well as nucleotides 211–212 (the A-rich bulge/P4 A-minor interaction), a transition we term $I_{TL\text{-}TR}$-to-F (Scheme 2; Fig. 2). In Mg^{2+}, these protections appear with a midpoint of 0.24 ± 0.01 mM, whereas in Mn^{2+} the corresponding protections appear at a fourfold lower concentration (0.06 ± 0.01 mM), indicating significant Mn^{2+}-specific stabilization (Fig. 3A; Table 1). Both in Mg^{2+} and Mn^{2+}, transitions occur with a Hill coefficient of approximately two (e.g., 1.8 ± 0.2 for both Mg^{2+} and Mn^{2+} titrations monitored at nucleotide

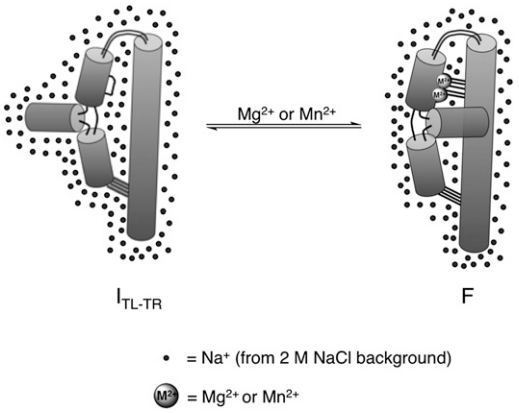

FIGURE 2. Model for equilibrium Mg^{2+}- or Mn^{2+}-induced folding of unmodified P4–P6 in a background of 2 M NaCl, which promotes the formation of a subset of long-range tertiary interactions. Two Mg^{2+} or Mn^{2+} ions bind within the A-rich bulge to form the final folded structure. (Adapted from Das et al. 2005b with permission from American Chemical Society © 2005.)

164; Table 1; Supplemental Table S1), consistent with prior work that demonstrated binding of two metal ions to induce formation of the fully folded state in 2 M NaCl (Das et al. 2005b; Travers et al. 2007).

The observation that Mn^{2+} aids folding of P4–P6 even in the absence of phosphorothioate substitutions raised the possibility that prior findings of "anomalous" rescue of outer-sphere metal-ion interactions arose from this enhanced overall stability and not from a specific ability of Mn^{2+} to rescue outer sphere interactions. We therefore revisited these crystallographic outer-sphere ligands with a thermodynamically rigorous approach, focusing on the *pro-*R_P nonbridging oxygen atoms of G188 or G163. Prior analog-interference analyses have shown that sulfur substitution at either of these sites disrupts folding in 2 mM Mg^{2+} and low concentrations of monovalent cations, as measured by native gel electrophoresis (Cate et al. 1997; Basu and Strobel 1999). Inclusion of 0.3 mM Mn^{2+} with 1.7 mM Mg^{2+} induced an apparent rescue of folding at both of these sites (Basu and Strobel 1999). This rescue by inclusion of a small amount of Mn^{2+} was taken as evidence for an ability of Mn^{2+} to rescue outer-sphere metal-ion interactions, a highly unexpected result as noted above. The single "rescuing" metal-ion mixture was chosen because it did not suppress folding interference of a nonmetal site phosphorothioate (A139 R_P PS) and several 2′-deoxy interference sites. The mixture therefore was thought to minimize any nonspecific stabilizing effects of Mn^{2+}. However, no attempt was made to measure nonspecific stabilizing effects of Mn^{2+} on the folding of unmodified P4–P6, the comparison species for which nonspecific Mn^{2+} effects would have meaning in the experiment. In effect, the prior study used A139 R_P PS and the 2′-deoxy interferences as substitutes for unmodified P4–P6, whose folding behavior in Mn^{2+} was never assessed.

Hydroxyl radical footprinting for G188 R_P PS gave protections at a sevenfold higher Mg^{2+} midpoint (1.66 ± 0.05 mM) relative to unmodified P4–P6 (Fig. 3B; Table 1). For G163 R_P PS, the protections appeared at a twofold higher Mg^{2+} midpoint (0.46 ± 0.06 mM) relative to unmodified P4–P6 (Fig. 3C; Table 1). These results indicate that sulfur substitution of either putative outer-sphere ligand destabilizes folding, and that increasing the Mg^{2+} concentration can overcome the effects of the substitution. Saturating Mg^{2+} induced the same protection patterns in G188 R_P PS and G163 R_P PS as for unmodified P4–P6, indicating that at the resolution of the assay, neither substitution changes the folded P4–P6 structure (data not shown).

The corresponding Mn^{2+} midpoints for the protections for G188 R_P PS and G163 R_P PS P4–P6 in 2 M NaCl were 0.32 ± 0.01 mM and 0.11 ± 0.01 mM, respectively (Fig. 3B,C; Table 1). The two modifications increased the midpoint for folding in Mn^{2+} by fivefold and twofold, respectively, nearly the same effects as in Mg^{2+} (ratios of sevenfold and twofold, respectively) (Fig. 3B,C; Table 1). Thus, there is no specific Mn^{2+} rescue of the outer-sphere phosphorothioates under these conditions. Instead, compared with Mg^{2+}, Mn^{2+} has a nonspecific and similar stabilizing effect for the unmodified RNA and its variants with outer-sphere phosphorothioates. This conclusion is rendered more quantitative and precise by taking into account lowered apparent Hill coefficients for the mutants (see Table 1) within the thermodynamic framework described in the next section. In particular, Model 1 and Scheme 3 below provide a physical explanation for the change in the apparent Hill coefficient for the variants under these conditions.

We next investigated whether Mn^{2+} could rescue folding of P4–P6 RNAs bearing phosphorothioate substitutions of inner-sphere Mg^{2+} ligands. We focused on A184, whose nonbridging oxygens make inner-sphere contacts to each of the A-rich bulge's metal ions in crystallographic models (Fig. 1C, left). Sulfur substitution of the *pro-*R_P oxygen of A184 interfered with P4–P6 folding using the aforementioned native gel assay (Cate et al. 1997; Basu and Strobel 1999). Neither Mn^{2+} nor other soft metal ions suppressed this folding interference under the single assay condition used previously (Basu and Strobel 1999). Sulfur substitution of the *pro-*S_P oxygen of A184 has not been reported. We constructed three P4–P6 RNAs with phosphorothioate substitutions of the *pro-*R_P, *pro-*S_P, or both (phosphorodithioate, PS_2) nonbridging oxygens of A184 (Supplemental Fig. S1).

In 2 M NaCl, the Mg^{2+}- and Mn^{2+}-induced protection patterns for A184 R_P PS, A184 S_P PS, and A184 PS_2 RNAs closely resemble those of unmodified P4–P6 (data not shown). This similarity suggests that the folded structures of these inner-sphere mutants closely resemble the structure of unmodified P4–P6 RNA. However, the phosphorothioate substitution of either or both of the nonbridging

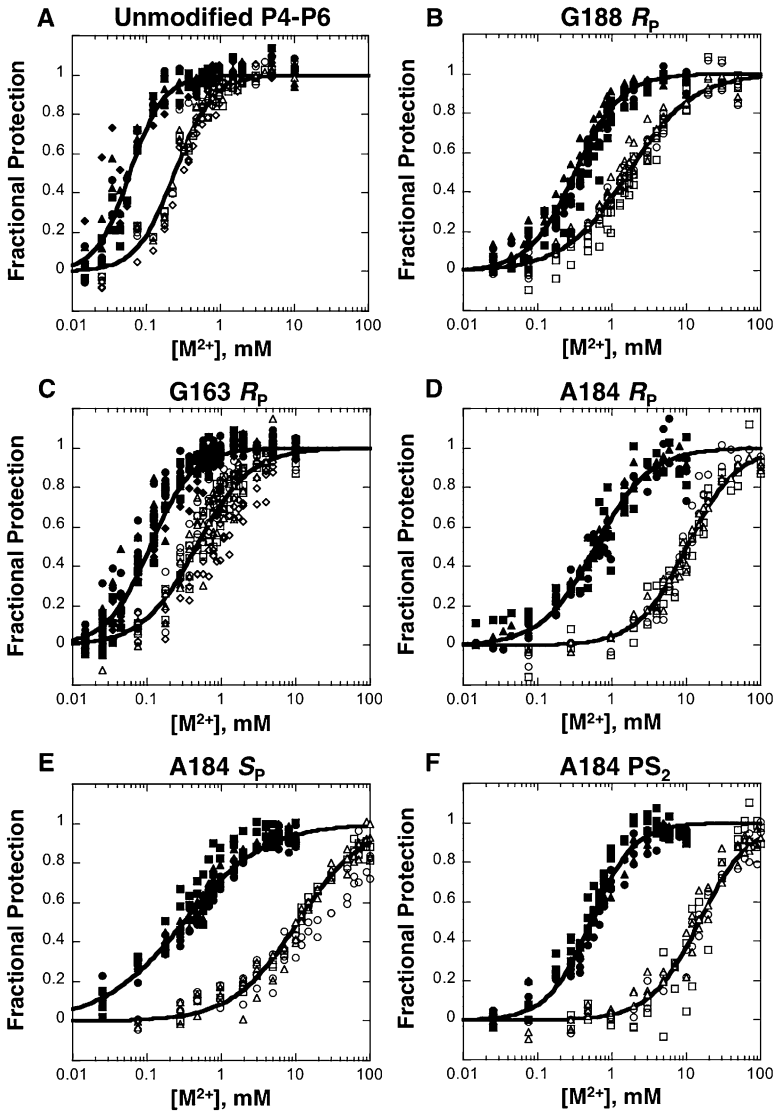

FIGURE 3. Equilibrium Mg^{2+}- and Mn^{2+}-induced folding of unmodified P4–P6 (*A*) and phosphorothioate-substituted variants (*B–F*) in a background of 2 M NaCl (with 50 mM Na-MOPS at pH 7). Mg^{2+} data points are shown as open symbols and Mn^{2+} data points are shown as closed symbols. Values of the fractional protection from hydroxyl radical cleavage derived from two to four independent experiments for subdomain nucleotides 164 (triangles), 176–177 (circles), 180–182 (squares), and 187 (diamonds) were averaged according to the procedure outlined in the Materials and Methods and Supplemental Material. The resulting values were fit to the Hill equation to yield curves whose midpoints and Hill coefficients reflect the appearance of protections over all of the protected nucleotides simultaneously. Data for nucleotide 187 are not included for certain variants due to nonspecific degradation of the phosphorothioate linkage, which interfered with the protection signal at this site.

oxygens of A184 destabilized Mg^{2+}-induced P4–P6 folding dramatically compared with unmodified P4–P6, with the Mg^{2+} midpoints associated with the appearance of protections occurring at 43-, 44-, and 63-fold higher Mg^{2+} concentrations than unmodified P4–P6 (Fig. 3A,D–F; Table 1). In Mn^{2+}, the folding midpoints for the three inner-sphere constructs increase by 10-, five-, and ninefold relative to the unmodified RNA (Fig. 3A,D–F; Table 1). The ratios of these Mg^{2+} and Mn^{2+} midpoints give apparent fold rescue values of 4, 9, and 7, respectively, much greater than the values of near unity obtained for the outer-sphere substitutions (Fig. 4A).

These results suggest that Mn^{2+} specifically rescues folding of A184 R_P PS, A184 S_P PS, and A184 PS_2 relative to unmodified P4–P6, a result that is typically taken as evidence for inner-sphere coordination between Mn^{2+} and the phosphorothioate, and is consistent with the crystal structure of P4–P6 with Mg^{2+} and unsubstituted phosphates (Fig. 1; Cate et al. 1996; Juneau et al. 2001). These results further suggest that the two divalent metal ions that bind cooperatively with P4–P6 folding in the 2 M NaCl background are the metal ions that make inner-sphere interactions with the phosphoryl oxygen atoms of residue A184. Nevertheless, the apparent Hill coefficients are different for different variants (Table 1; Supplemental Fig. S2); thus, as noted above, "fold-rescue" values do not report directly on ΔΔΔG (i.e., Equations 3 and 4 are invalid) and, at best, give a qualitative summary of the results. To make basic conclusions about the energetic significance of these effects, a thermodynamic framework for computing the free-energy differences of metal-ion rescue is necessary. Such a framework is discussed next.

Thermodynamic models consistent with the rescue data

Estimating free-energy differences from the Mg^{2+} and Mn^{2+} titration data for the P4–P6 RNA and its variants requires extending the "standard" thermodynamic framework in Equations 1–4, which assumes that Hill coefficients for different RNAs are constant at different divalent metal-ion concentrations. In particular, the fitted Hill coefficients for the thio-modified variants are systematically lower than the values of ~2 for the unmodified RNA (Table 1; Supplemental Table S1; Supplemental Fig. S2) and, indeed, decrease to values near 1 for the more destabilized variants (Table 1; Supplemental Table S1). We therefore sought simple extensions of the thermodynamic framework (Weiss 1997; Garcia et al. 2011) that model changing Hill slopes, while still permitting extraction of well-defined ΔΔG and ΔΔΔG values for evaluating metal-ion

TABLE 1. Mg^{2+}- and Mn^{2+}-dependent folding of P4–P6 in 2 M NaCl

		Weighted average across residues 164–187 (P5abc subdomain)			
Construct	Ligand type	$[Mg^{2+}]_{1/2}$ (mM)	n_{Hill}	$[Mn^{2+}]_{1/2}$ (mM)	n_{Hill}
Unmodified		0.24 ± 0.01	1.7 ± 0.1	0.06 ± 0.01	1.9 ± 0.1
G188 R_P	OS	1.66 ± 0.05	1.0 ± 0.1	0.32 ± 0.01	1.4 ± 0.1
G163 R_P	OS	0.46 ± 0.06	1.2 ± 0.1	0.11 ± 0.01	1.5 ± 0.1
A184 R_P	IS	10.2 ± 0.6	1.3 ± 0.1	0.60 ± 0.05	1.2 ± 0.1
A184 S_P	IS	10.6 ± 0.3	1.0 ± 0.1	0.31 ± 0.04	0.8 ± 0.1
A184 PS_2	IS	15 ± 2	1.3 ± 0.1	0.52 ± 0.02	1.5 ± 0.1

rescue. We explored two such models and found them to give numerical free-energy differences for the data herein that were indistinguishable within experimental error.

Model 1. Two site-bound metal ions derived from solution or from the atmosphere

The data herein and from previous work are well fit by a model in which $I_{TL\text{-}TR}$-to-F folding of unmodified P4–P6 is associated with the specific site binding of two divalent metal ions brought in from solution (Scheme 2). Due to the large excess of Na^+ saturating the atmosphere (cf. solution concentrations of 2 M NaCl with submillimolar $MgCl_2$ or $MnCl_2$), the number of "atmospheric" divalent metal ions is assumed to be either negligible or similar in the $I_{TL\text{-}TR}$ and F states and, indeed, the number of these background ions was verified to be one or less by direct ion counting (Das et al. 2005b). Scheme 2 does not show these diffusely bound divalent metal ions, sodium ions, or chloride ions, as they are negligible in the thermodynamic formulas describing the titration (Equations 1 and 2, with $n = 2$). However, for the destabilized thio-modified variants herein, higher concentrations of divalent ions are required to probe the $I_{TL\text{-}TR}$-to-F transition, raising the possibility that some atmospheric divalent metal ions might be present in $I_{TL\text{-}TR}$ under these conditions and that these metal ions might enter the metal-ion core upon folding to F. Because we assumed that F contains a maximum of two site-bound ions, we considered the possibility that $I_{TL\text{-}TR}$ preassociates with a single metal ion to form $I_{TL\text{-}TR}{\bullet}M^{2+}$ according to a separate equilibrium constant, K_1 (Scheme 3). We also considered a model with two metal ions preassociated with $I_{TL\text{-}TR}$ to form an additional species ($I_{TL\text{-}TR}{\bullet}2M^{2+}$); a significant fraction of such a species would lead to an admixture of $I_{TL\text{-}TR}$ and F at high divalent metal-ion concentrations. As we observe hydroxyl radical reactivities consistent with complete folding of all the RNAs herein, we do not include such a species. According to Scheme 3, folding to $F{\bullet}2M^{2+}$ occurs either from the $I_{TL\text{-}TR}$ species via K_2, or from $I_{TL\text{-}TR}{\bullet}M^{2+}$.

To apply Scheme 3 to the metal-ion rescue experiments, we assumed that the second equilibrium, which involves folding from $I_{TL\text{-}TR}{\bullet}M^{2+}$ to form $F{\bullet}2M^{2+}$ via binding of a second divalent metal ion, was perturbed by the assayed thio modifications. We also assumed that the first equilibrium—binding of an "extra" metal ion to $I_{TL\text{-}TR}$ with equilibrium constant K_1—was the same for all mutants, as would be expected if this metal ion was diffusely associated with the RNA and if all variants had similar structural ensembles in the metal core-free $I_{TL\text{-}TR}$ state. Equations for fraction folded, free energies, and M^{2+}-dependent Hill coefficients are given in the Supplemental Material. The model predicts that if a variant folds with a midpoint $[M^{2+}]_{1/2}$, its apparent Hill coefficient is

$$n = 2 - \left(\frac{\frac{[M^{2+}]}{K_1}}{1 + \frac{[M^{2+}]}{K_1}} \right). \quad (5)$$

This equation gives a Hill coefficient of 2 for stable variants, monotonically decreasing to 1 for destabilized variants, resulting from preassociation of a single metal ion with $I_{TL\text{-}TR}$ at higher divalent metal-ion concentrations as prescribed by the model. This model accounts for the entire Mg^{2+} and Mn^{2+} data sets of unmodified P4–P6 and the five variants (Fig. 5, solid lines), with K_1 values of 0.26 ± 0.16 mM (Mg^{2+}) and 0.13 ± 0.08 mM (Mn^{2+}). This global fit then permits quantitative evaluation of the free-energy differences and metal-ion rescue for each P4–P6 thio substitution (Table 2).

For the putative outer-sphere ligand modifications, the Mg^{2+}-dependent folding transition $I_{TL\text{-}TR}$-to-F was destabilized by ΔΔG values of 1.49 ± 0.15 kcal/mol and 0.55 ± 0.13 kcal/mol for G188 R_P PS and G163 R_P PS, respectively (Table 2). When folded in Mn^{2+}, the destabilization ΔΔG values for these two variants were 1.47 ± 0.23 kcal/mol and 0.58 ± 0.20 kcal/mol, indistinguishable from the Mg^{2+} values, given experimental error. The metal-ion rescue free-energy values ΔΔΔG were obtained by subtracting the Mg^{2+} and Mn^{2+} ΔΔG values and gave 0.02 ± 0.28 kcal/mol and −0.02 ± 0.24 kcal/mol for G188 R_P PS and G163 R_P PS, respectively. Both values were indistinguishable from zero ($P = 0.5$). This analysis indicates that substituting phosphorothioates for these crystallographically observed outer-sphere ligands in the P4–P6 system results in negligible metal-ion rescue.

For the putative inner-sphere ligand modifications A184 R_P PS, A184 S_P PS, and A184 PS_2, this framework gave

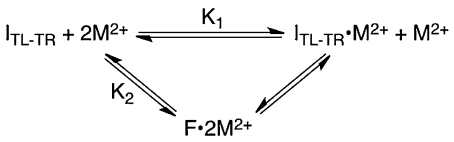

SCHEME 3.

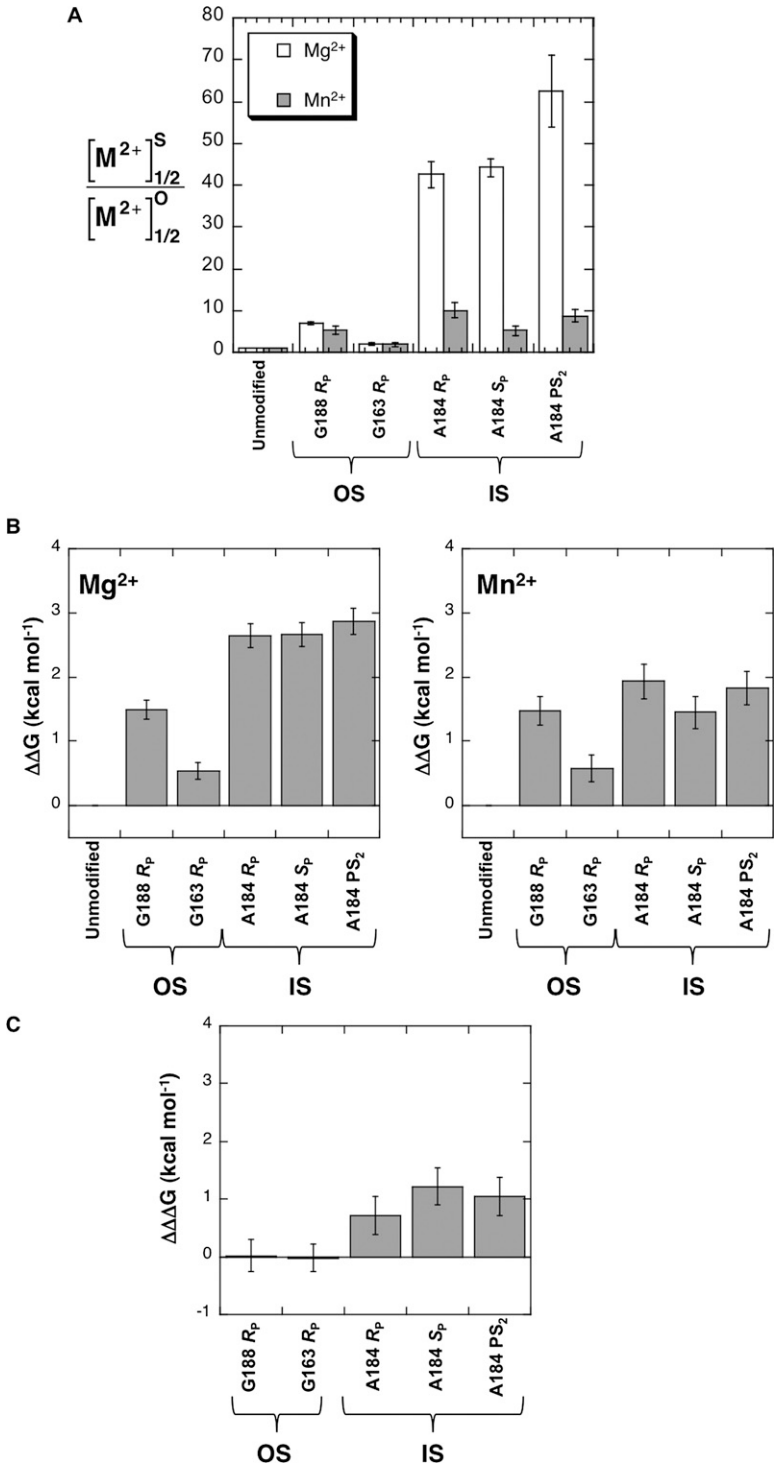

FIGURE 4. (*A*) Divalent metal-ion midpoint ratios of P4–P6 variants folded in either Mg^{2+} or in Mn^{2+} in a background of 2 M NaCl (OS: outer-sphere metal-ion ligand; IS: inner-sphere metal-ion ligand). (*B*) Calculated ΔΔG values (relative to unmodified P4–P6) associated with Mg^{2+}-induced (*left*) and Mn^{2+}-induced (*right*) folding of P4–P6 phosphorothioate variants with respect to unmodified P4–P6. The values were calculated according to a thermodynamic framework in which two site-bound metal ions, derived from solution or from the ion atmosphere, bind within the metal-ion core (Model 1, Supplemental Material). (*C*) Calculated ΔΔΔG values associated with Mg^{2+}- vs. Mn^{2+}-induced folding of phosphorothioate-subsituted P4–P6 variants in a background of 2 M NaCl.

ΔΔG values of 2.64 ± 0.19 kcal/mol, 2.66 ± 0.19 kcal/mol, and 2.87 ± 0.21 kcal/mol for A184 R_P PS, A184 S_P PS, and A184 PS_2, respectively, for the folding transition $I_{TL\text{-}TR}$-to-F induced by Mg^{2+} (Table 2). In contrast to the outer-sphere ligand experiments above, the ΔΔG values for folding in Mn^{2+} were lower: 1.93 ± 0.27, 1.45 ± 0.25, and 1.83 ± 0.26 kcal/mol. Thus, the results suggest metal-ion rescue, with rescue free-energy values of ΔΔΔG of 0.71 ± 0.33 kcal/mol, 1.22 ± 0.32 kcal/mol, and 1.04 ± 0.33 kcal/mol for A184 R_P PS, A184 S_P PS, and A184 PS_2, respectively. The results give strong evidence for nonzero metal-ion rescue for both A184 nonbridging oxygens ($P = 0.02$, $P = 7 \times 10^{-5}$, and $P = 8 \times 10^{-4}$ for A184 R_P PS, A184 S_P PS, and A184 PS_2, respectively), consistent with their observation as inner-sphere metal-ion ligands in the crystallographic analysis of P4–P6. Figure 4B shows the free energy differences (ΔΔG) for folding in both Mg^{2+} and Mn^{2+} in graphic form, while Figure 4C shows the rescue factors (ΔΔΔG) associated with each phosphorothioate construct.

Model 2. Linear expansion of the apparent Hill coefficient

Model 1 posits a functional form for how the free-energy difference ΔG for an RNA conformational transition varies with background divalent metal-ion concentration and assumes that each RNA modification perturbs this relationship by some constant ΔΔG. However, the model makes use of the special conditions of the experiment (high background sodium ion concentration) and assumptions specific to the P4–P6 metal core transition ($I_{TL\text{-}TR}$-to-F) to derive the relevant thermodynamic relations. To support the above analysis and to enable analysis under different monovalent ion background conditions (see below), we also explored a framework in which the expression for the free energy was assumed to take a more general form, and in which the data on the unmodified and thio-modified RNA were used to carry out a local mathematical expansion of

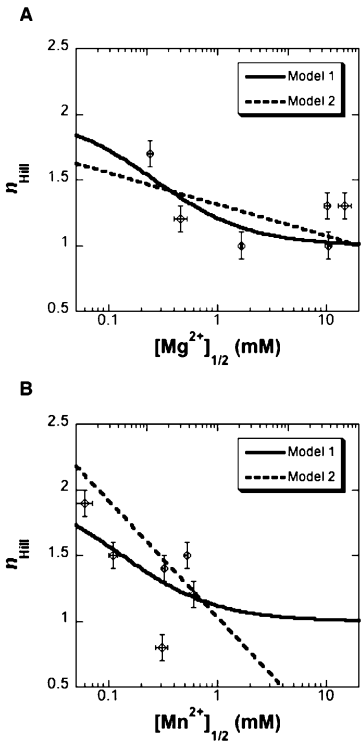

FIGURE 5. Curves describing the variation of the Hill coefficient (n_{Hill}) with the divalent metal-ion folding midpoint according to models 1 (solid lines; see equation 5) and 2 (dashed lines; see equation 6) for folding of P4–P6 variants in Mg^{2+} (*A*) and in Mn^{2+} (*B*) in a background of 2 M NaCl. The data points are the experimentally estimated values of n_{Hill} and $[M^{2+}]_{1/2}$ for each individual RNA construct (Table 1).

the free energy as a function of metal-ion concentration. This framework has been applied previously to analyze the thermostabilization of a signal recognition particle RNA motif by substitutions predicted by the Rosetta design algorithm (Das et al. 2010).

Explicitly, we carried out the mathematical expansion on the apparent Hill coefficient function $n([M^{2+}])$, which is proportional to the derivative of $\Delta G([M^{2+}])$ with respect to $\ln[M^{2+}]$ (see Supplemental Material). This expansion does not require assumptions of high background monovalent ion concentrations or discreteness of the metal-ion binding sites, and thus is applicable as described below to conformational transitions that occur under low monovalent salt concentrations, which are more commonly encountered. We assumed that n varies smoothly with $[M^{2+}]$, as it does for computational models or direct measurements of ion atmospheres around fixed or changing RNA conformational ensembles (Manning 1977a,b; Anderson and Record 1990; Bai et al. 2007; Leipply and Draper 2010). We then confirmed that a simple linear expansion fits the observed apparent Hill coefficients herein (Fig. 5, dashed lines):

$$n\left([M^{2+}]\right) = n_0 + \alpha_n \ln\left[\frac{[M^{2+}]}{\left([M^{2+}]_{1/2}\right)_0}\right]. \quad (6)$$

Here, n_0, the apparent Hill coefficient of the unmodified RNA near its folding midpoint, and the coefficient α_n are fitted parameters, and $\left([M^{2+}]_{1/2}\right)_0$ is the folding midpoint of the unmodified construct. Note that the values of the fitted parameters depend on the different folding midpoints and Hill coefficients of each individual RNA variant (the data points in Fig. 5). The model therefore makes no assumptions about the values of the Hill coefficients, which retain their experimentally determined values.

The corresponding equations for free-energy differences (derived in the Supplemental Material) gave ΔΔG values for all phosphorothioate modifications in both Mg^{2+} and Mn^{2+} that were within error of the values computed using Model 1 above (Table 2). In particular, the final metal-ion rescue values ΔΔΔG were calculated to be 0.37 ± 0.35 kcal/mol ($P = 0.1$), 0.06 ± 0.29 kcal/mol ($P = 0.4$), 1.34 ± 0.61 kcal/mol ($P = 0.01$), 1.72 ± 0.58 kcal/mol ($P = 0.002$), and 1.68 ± 0.66 kcal/mol ($P = 0.005$) for the modifications G188 R_P PS, G163 R_P PS, A184 R_P PS, A184 S_P PS, and A184 PS_2, respectively. These values are indistinguishable within experimental error from those obtained using Model 1 above, and further support the conclusion that metal-ion rescue is negligible for outer-sphere sites, but significant for inner-sphere ligands.

Testing rescue of P4–P6 folding in low background Na^+ concentration

The above experiments carried out in 2 M NaCl support the conceptual underpinnings of metal-ion rescue experi-

TABLE 2. Folding free energy differences of unmodified vs. phosphorothioate-substituted P4–P6 in 2 M NaCl

Construct	Ligand type	Model	ΔΔG (kcal mol^{-1}) Mg^{2+}	ΔΔG (kcal mol^{-1}) Mn^{2+}	ΔΔΔG (kcal mol^{-1})
G188 R_P	OS	1	1.49 ± 0.15	1.47 ± 0.23	0.02 ± 0.28
		2	1.54 ± 0.23	1.17 ± 0.27	0.37 ± 0.35
G163 R_P	OS	1	0.55 ± 0.13	0.58 ± 0.20	−0.02 ± 0.24
		2	0.53 ± 0.13	0.47 ± 0.26	0.06 ± 0.29
A184 R_P	IS	1	2.64 ± 0.19	1.93 ± 0.27	0.71 ± 0.33
		2	2.85 ± 0.50	1.50 ± 0.35	1.34 ± 0.61
A184 S_P	IS	1	2.66 ± 0.19	1.45 ± 0.25	1.22 ± 0.32
		2	2.87 ± 0.51	1.15 ± 0.28	1.72 ± 0.58
A184 PS_2	IS	1	2.87 ± 0.21	1.83 ± 0.26	1.04 ± 0.33
		2	3.11 ± 0.57	1.43 ± 0.32	1.68 ± 0.66

Model 1: Two site-bound metal ions derived from solution or from the atmosphere.
Model 2: Linear expansion of the apparent Hill coefficient.

ments and indicate that, with proper thermodynamic comparisons, the approach can specifically identify site-bound metal ions within folded RNAs. To more directly compare these results with those obtained by Basu and Strobel (1999), to reveal another complexity in thermodynamic analyses, and to demonstrate how this complexity can be identified and addressed, we have carried out hydroxyl radical footprinting of the constructs described above in low background Na^+ concentration. We first describe the results in the absence of phosphorothioate substitutions, as these results reveal a critical new feature in the P4–P6 folding pathway.

Mg^{2+}- and Mn^{2+}-induced folding of unmodified P4–P6 in low background Na^+ concentration

For P4–P6 folding in low-background monovalent cation concentration, in contrast to the behavior in 2 M NaCl, the RNA initially lacks all of the tertiary interactions, so that extensive three-dimensional structure forms as Mg^{2+} or Mn^{2+} is added. Under these conditions, P4–P6 folds in Mg^{2+} via an apparent single cooperative transition (U-to-F) (Fig. 6A, left). All of the hydroxyl radical protections arise over a narrow Mg^{2+} concentration range, with an average midpoint and apparent Hill coefficient of 0.42 ± 0.01 mM and 4.2 ± 0.1, respectively (Fig. 6B, left; Table 3A). These values agree with those obtained for P4–P6 folding in low background monovalent cation concentration monitored by native gel electrophoresis ($[Mg^{2+}]_{1/2}$ = 0.46 mM, $n_{Hill} \sim 4$) (Juneau et al. 2001; Schwans et al. 2003), which monitors global molecular compaction.

In contrast, P4–P6 folds via two transitions when Mn^{2+} is used as the divalent metal ion. A subset of the protections (152–153 and 200–202) appears at a slightly lower midpoint than in Mg^{2+}, but protections of other residues (176–177 and 180–182) occur at a 10-fold lower Mn^{2+} concentration (Fig. 6B, right; Table 3B). The residues that are protected at the lower Mn^{2+} concentration (closed squares) correspond to a previously identified folding subdomain, P5abc, which can adopt structure independent of the overall P4–P6 structure (Murphy and Cech 1993; Wu and Tinoco 1998; Silverman et al. 1999; Zheng et al. 2001). Thus, the first protections that appear with increasing Mn^{2+} concentration correspond to a previously unseen U-to-I_{P5abc} transition. The protections that arise at higher Mn^{2+} concentrations correspond to formation of the tertiary interactions between the two sets of coaxially stacked helices in the folded P4–P6 structure (I_{P5abc}-to-F) (Fig. 6B, closed circles; Fig. 1A,B). This three-state, two-transition folding model shown in the right panel of Figure 6A is supported by results with a P4–P6 mutant in which J5/5a is base paired to prevent formation of the overall tertiary structure. This mutant gives P5abc folding at low Mn^{2+} concentration as observed within the context of unmodified P4–P6, but requires considerably higher Mg^{2+} concentrations than unmodified P4–P6 to support acquisition of the final tertiary structure (Murphy and Cech 1994; Wu and Tinoco 1998; data not shown). The prior work using gel electrophoretic measurements (Basu and Strobel 1999; Silverman and Cech 1999; JK Frederiksen and JH Piccirilli, unpubl.) did not detect the U-to-I_{P5abc} transition, possibly because the structural change is too subtle to be detected at the resolution of a gel mobility assay.

Thus, in 20 mM Na^+, acquisition of the final tertiary structure requires similar concentrations of Mg^{2+} and Mn^{2+}, but the underlying process or folding mechanism is distinct, with Mn^{2+} promoting formation of a predominant folding intermediate that contains the two identified metal-ion binding sites (Fig. 6A, right). This difference has profound consequences. Whereas modifications that significantly weaken Mg^{2+} affinity for these binding sites would result in an increased $[Mg^{2+}]_{1/2}$ for overall tertiary folding, the same modification in Mn^{2+} might have no influence on the $[Mn^{2+}]_{1/2}$ for overall tertiary folding. In other words, a modification that increases the $[Mn^{2+}]_{1/2}$ for formation of the subdomain (which contains the metal-ion binding sites) by ~10-fold would still allow metal-ion binding and subdomain formation at a Mn^{2+} concentration below that required for formation of the overall tertiary structure (Fig. 6B, open vs. closed symbols) so that no shift in $[Mn^{2+}]_{1/2}$ for the overall tertiary structure formation would be observed.

Because of the different folding pathways, any mutation or modification that uniformly perturbed the $[M^{2+}]_{1/2}$ for the single folding transition in Mg^{2+} and for subdomain formation in Mn^{2+}, such as modification of an outer-sphere ligand, would give apparent rescue in gel mobility measurements, which monitor only overall tertiary structure formation (i.e., the ratio $[Mn^{2+}]_{1/2}/[Mg^{2+}]_{1/2}$ would decrease for thio-substituted P4–P6 relative to wild-type P4–P6). Further, rescue of inner-sphere metal-ion ligand perturbations would not be apparent at only a single rescuing Mn^{2+} concentration, as was used in the prior study (Basu and Strobel 1999), if the added Mn^{2+} were insufficient to overcome a strong destabilizing effect from disruption of these metal-ion interactions.

Mg^{2+}- and Mn^{2+}-induced folding of phosphorothioate-substituted P4–P6 in 20 mM Na^+

We first investigated folding of the two outer-sphere phosphorothioate-substituted P4–P6 RNAs, G188 R_P PS and G163 R_P PS, in the 20 mM Na^+ background (Fig. 6C,D). With sufficient Mg^{2+}, both constructs yield the same protection patterns as unmodified P4–P6 (left). Subdomain and tertiary protections for the phosphorothioates (open squares and open circles, respectively) appear over a narrow Mg^{2+} concentration range, analogous to the apparent single cooperative folding transition observed for unmodified P4–P6 in Mg^{2+}, but at approximately twofold higher Mg^{2+} midpoints and with lower apparent Hill coefficients compared with unmodified P4–P6, reflecting decreased folding stability (Table 3A).

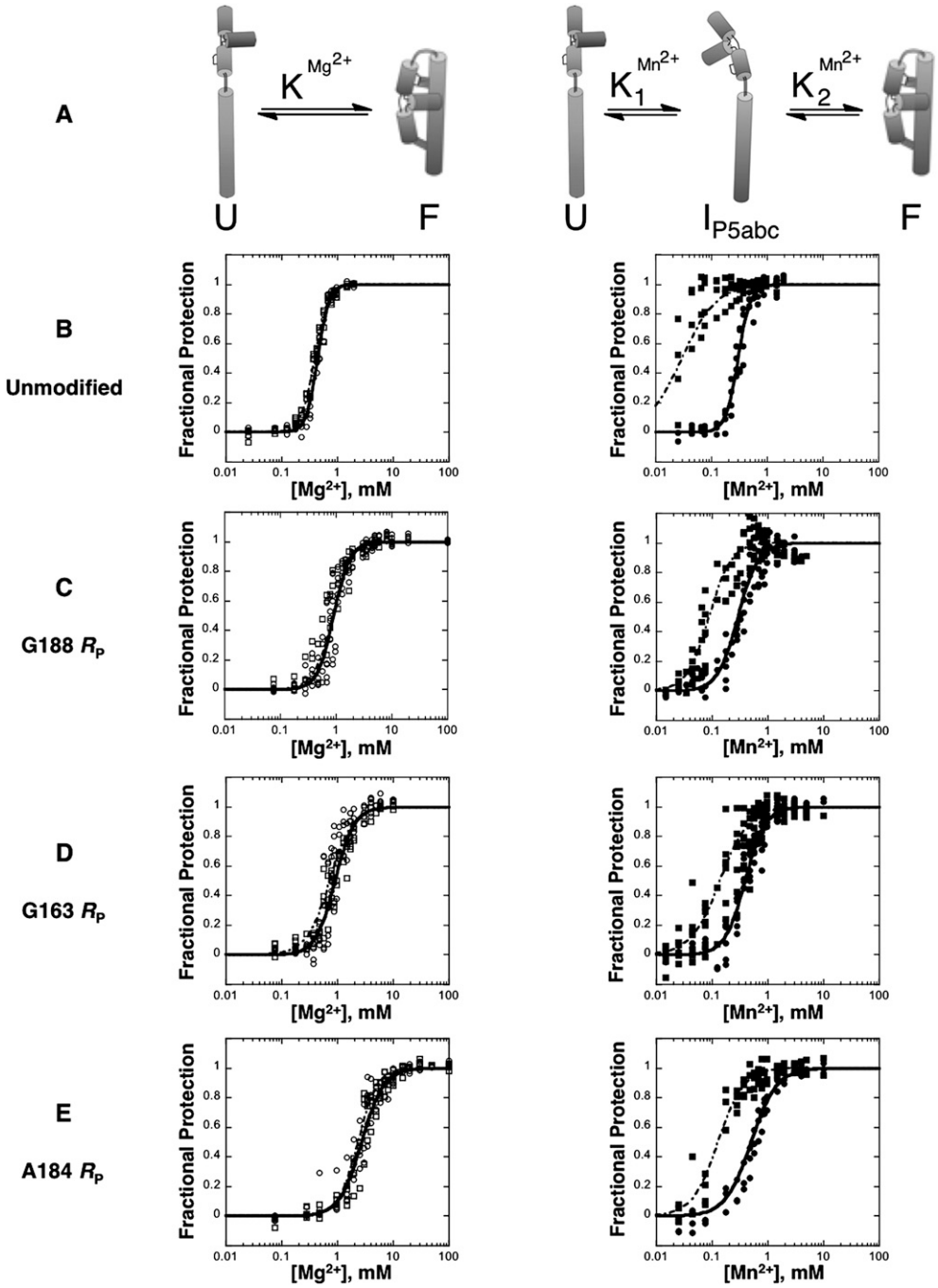

FIGURE 6. (Continued on next page)

In Mn^{2+}, these modified P4–P6 RNAs exhibit separate folding transitions for subdomain formation and overall tertiary structure formation, as is observed for the unmodified RNA (Fig. 6C,D, right). The $[Mn^{2+}]_{1/2}$ value for formation of the subdomain is increased relative to unmodified P4–P6, but formation of the final tertiary structure is not significantly affected (Fig. 6C,D, right; Tables 3A, 3B). Even though the subdomain is destabilized, it still folds at concentrations lower than those required for overall tertiary folding, so the overall tertiary folding of these variants is unaffected (Table 3B) ($[Mn^{2+}]_{1/2}$ = 0.3–0.4 mM). Thus, a destabilizing effect on formation of the subdomain manifests as an effect on acquisition of overall tertiary structure in Mg^{2+}, as folding of the subdomain is coupled to overall folding in Mg^{2+}, but has no effect on overall folding in Mn^{2+} because subdomain folding is complete at

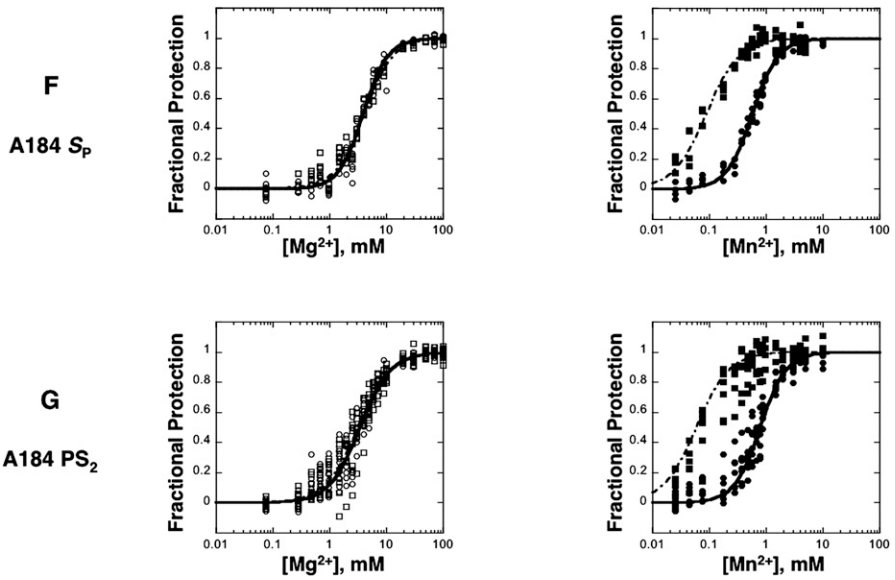

FIGURE 6. Mg^{2+}- or Mn^{2+}-induced folding of P4–P6 variants in a background of 20 mM Na^+. Folding of unmodified P4–P6 in Mg^{2+} follows an apparent two-state transition modeled as U-to-F (*A*, *left*), in which both subdomain protections (*B–G*, *left*, open squares and dashed curves) and tertiary protections (*B–G*, *left*, open circles and solid curves) appear over approximately the same Mg^{2+} concentration range. In contrast, folding in Mn^{2+} follows the three-state transition U-to-I_{P5abc}-to-F (*A*, *right*), in which the subdomain protections (*B–G*, *right*, closed squares and dashed curves) appear at lower concentrations than the protections associated with formation of tertiary structure (*B–G*, *right*, closed circles and solid curves). Data points and curve fits were obtained for the subdomain and tertiary protections analogously to the procedure described for Figure 3.

lower Mn^{2+} concentrations than overall tertiary structure formation (Fig. 6A). The destabilizing effect in Mg^{2+} and the absence of such an effect in Mn^{2+} corresponds to an apparent rescue of tertiary folding (Fig. 7A), but a rigorous appraisal requires accurately taking into account the additional intermediate observed in Mn^{2+}. Complexities from this previously unknown intermediate account for the small, but significant apparent rescue of these outer-sphere constructs observed previously by native gel mobility assays that monitor primarily the global compaction associated with tertiary folding (Basu and Strobel 1999). Analogously, metal-ion rescue of catalysis can be misleading if the same reaction steps are not monitored throughout the comparisons (Shan and Herschlag 2000; Hougland et al. 2005).

The three inner-sphere constructs (A184 R_P PS, A184 S_P PS, A184 PS_2) also exhibit the same regions of protection as unmodified P4–P6 when folded in a background of 20 mM Na^+ with sufficient divalent metal ion (data not shown). Like unmodified P4–P6, these constructs appear to fold in Mg^{2+} via a single transition, with subdomain and tertiary protections appearing over narrow concentration ranges (Fig. 6E–G, left; Table 3A). However, the associated midpoints occur at a six- to 10-fold higher Mg^{2+} concentration compared with unmodified P4–P6. As with the outer-sphere phosphorothioates, the increased folding midpoints reflect a destabilization of folding in Mg^{2+}, and the effects are greater than the effects from the outer-sphere thio substitutions (Fig. 7A).

Also as for the outer-sphere metal ions, the folding pathway in Mn^{2+} is different from that in Mg^{2+}, and this difference leads to apparent rescue. Figure 6E–G (right) shows the two transitions for folding in Mn^{2+}. As with the outer-sphere substitutions, the inner-sphere thio substitutions have a destabilizing effect on subdomain formation (closed squares) (cf. Fig. 6, C and D), but this transition still occurs at lower Mn^{2+} concentrations than tertiary folding (Fig. 6E–G, right, closed squares vs. closed circles), resulting in the observed subdomain folding intermediate. As described above for the outer-sphere thio substitutions, the higher $[Mg^{2+}]_{1/2}$ coupled with the absence of an effect on $[Mn^{2+}]_{1/2}$ for overall tertiary folding leads to apparent rescue (Fig. 7A). This apparent rescue is larger than that observed for the outer-sphere residues, but only because

TABLE 3A. Mg^{2+}-induced folding in 20 mM Na^+

		Subdomain		Tertiary	
Construct	Ligand type	$[Mg^{2+}]_{1/2}$ (mM)	n_{Hill}	$[Mg^{2+}]_{1/2}$ (mM)	n_{Hill}
Unmodified		0.40 ± 0.01	3.6 ± 0.2	0.44 ± 0.01	4.3 ± 0.1
G188 R_P	OS	0.88 ± 0.09	2.6 ± 0.9	0.9 ± 0.1	3.0 ± 0.7
G163 R_P	OS	0.74 ± 0.09	2.1 ± 0.2	0.9 ± 0.1	2.5 ± 0.3
A184 R_P	IS	2.38 ± 0.05	2.5 ± 0.1	2.7 ± 0.6	2.2 ± 0.4
A184 S_P	IS	4.1 ± 0.1	1.7 ± 0.3	3.9 ± 0.2	2.0 ± 0.1
A184 PS_2	IS	3.2 ± 0.5	1.5 ± 0.5	3.4 ± 0.5	1.6 ± 0.3

TABLE 3B. Mn^{2+}-induced folding in 20 mM Na^+

		Subdomain		Tertiary	
Construct	Ligand type	$[Mn^{2+}]_{1/2}$ (mM)	n_{Hill}	$[Mn^{2+}]_{1/2}$ (mM)	n_{Hill}
Unmodified		0.03 ± 0.01	1.4 ± 0.2	0.30 ± 0.03	3.9 ± 0.2
G188 R_P	OS	0.09 ± 0.02	2.2 ± 0.3	0.29 ± 0.04	2.4 ± 0.8
G163 R_P	OS	0.14 ± 0.01	1.7 ± 0.2	0.39 ± 0.02	2.4 ± 0.8
A184 R_P	IS	0.13 ± 0.01	1.9 ± 0.7	0.50 ± 0.02	1.9 ± 0.1
A184 S_P	IS	0.09 ± 0.01	1.5 ± 0.1	0.57 ± 0.02	1.9 ± 0.1
A184 PS_2	IS	0.06 ± 0.01	1.5 ± 0.2	0.78 ± 0.09	1.9 ± 0.2

the inner-sphere substitutions have a larger destabilizing effect than do the outer-sphere substitutions. Any substitution or mutation that has a larger effect on subdomain formation without an additional destabilizing effect on the overall tertiary structure formation (i.e., affecting U-to-I_{P5abc} without affecting the I_{P5abc}-to-F transition) would give a still larger apparent rescue. The apparent rescue arises from the inappropriate thermodynamic comparison of folding that occurs via two different pathways—in Mg^{2+}, from U to F, and in Mn^{2+}, from I_{P5abc} to F—and, therefore, need not have any relationship to rescue via stronger Mn^{2+}–sulfur interactions.

As with the simpler 2 M NaCl data, quantitative evaluation of metal-ion rescue in lower monovalent salt concentration requires calculating and comparing free-energy differences induced by thio modification for identical states in both Mg^{2+} and Mn^{2+} (Scheme 1). To resolve the complexity associated with different transition pathways in Mg^{2+} and Mn^{2+}, we calculated free-energy differences for the same overall process U-to-F. To resolve complexities associated with changing apparent Hill coefficients in modified RNAs, we analyzed the data in the general thermodynamic framework derived above based on global fits of the Hill coefficient across all variants (model 2; see Fig. 8 for the corresponding n_{Hill} vs. $[M^{2+}]_{1/2}$ plots). The results of these analyses are summarized in Figure 7, B and C and Table 4, and demonstrate Mn^{2+} rescue of the inner- but not outer-sphere ligands.

Figure 7B shows the overall folding free energies (between states U-to-F) for each construct in Mg^{2+} and Mn^{2+}, taking into account the single-transition vs. two-transition thermodynamics in the two conditions, respectively. The values in Mg^{2+} (Fig. 7B, left; Table 4, Mg^{2+}, U-to-F) are obtained from the single folding isotherms shown in Figure 6, B–G (left). The values in Mn^{2+} (Fig. 7B, right; Table 4, Mn^{2+}) require summing the free energies from the two sets of folding isotherms (Fig. 6B–G, right), representing the U-to-I_{P5abc} step (closed squares and dashed lines) and the I_{P5abc}-to-F step (closed circles and solid lines) to yield the total free-energy difference for U-to-F. Figure 7C plots these differences in the folding free energies in Mg^{2+} vs. Mn^{2+} to allow rescue to be evaluated. As in the analysis of the simpler 2 M NaCl data above, similar values of $\Delta\Delta G$ in Mn^{2+} vs. Mg^{2+} were observed for the outer-sphere substitutions G188 R_P PS and G163 R_P PS, giving no evidence of metal-ion rescue. Further, smaller $\Delta\Delta G$ values in Mn^{2+} vs. Mg^{2+} for inner-sphere thio substitutions (A184 R_P PS, A184 S_P PS, A184 PS_2) provide thermodynamic evidence for rescue of inner-sphere metal-ion interactions in these experiments. The quantitative values for the metal rescue free-energy differences $\Delta\Delta\Delta G$ are 0.45 ± 0.58 ($P = 0.2$), −0.66 ± 0.63 ($P = 0.9$), 0.71 ± 0.67 ($P = 0.1$), 1.48 ± 0.65 ($P = 0.01$), and 1.34 ± 0.64 ($P = 0.02$) kcal mol^{-1} for the modifications G188 R_P PS, G163 R_P PS, A184 S_P PS, A184 R_P PS, and A184 PS_2, respectively (Table 4). These values have larger errors than the results obtained in the simplifying 2 M NaCl conditions (Table 2), due to the summation of free energies over an additional transition in the Mn^{2+} titrations. For one of the constructs (A184 R_P PS), we cannot yet ascertain whether the measured rescue effect is greater than its associated error. Nevertheless, given these errors, the values in low monovalent salt and high monovalent salt background are in agreement, providing evidence for congruence between these biochemical metal-ion dissection experiments and the inner-sphere/outer-sphere nature of the RNA ligands from crystallography.

SUMMARY AND IMPLICATIONS

Metal-ion rescue: Successes and lingering concerns

Metal-ion rescue experiments have provided a powerful experimental approach for developing models of catalysis by ribozymes and for evaluating the functional relevance of structural models (Wang et al. 1999; Hougland et al. 2006; Nelson and Uhlenbeck 2006). Elucidation of the network of interactions mediated by metal ions and their ligands within ribozyme active sites has relied on the assumption that sites of rescue reveal ligands that occupy the inner coordination sphere of the metal ion. This interpretation follows logically from the known stronger coordination of rescuing metal ions to sulfur than oxygen. While the absence of rescue, a negative result, cannot be used to provide evidence against a direct metal-ion interaction, and while rescue can occur from recruitment of a new interaction not present in the wild-type/cognate pair, metal-ion rescue experiments have been used extensively with functional RNAs, and the results have been predictive of further functional and structural results (Wang et al. 1999; Adams et al. 2004; Guo et al. 2004; Golden et al. 2005; Hougland et al. 2006; Nelson and Uhlenbeck 2006). For example, quantitative metal-ion rescue studies provided evidence for a single catalytic metal ion that bridged positions 20 Å

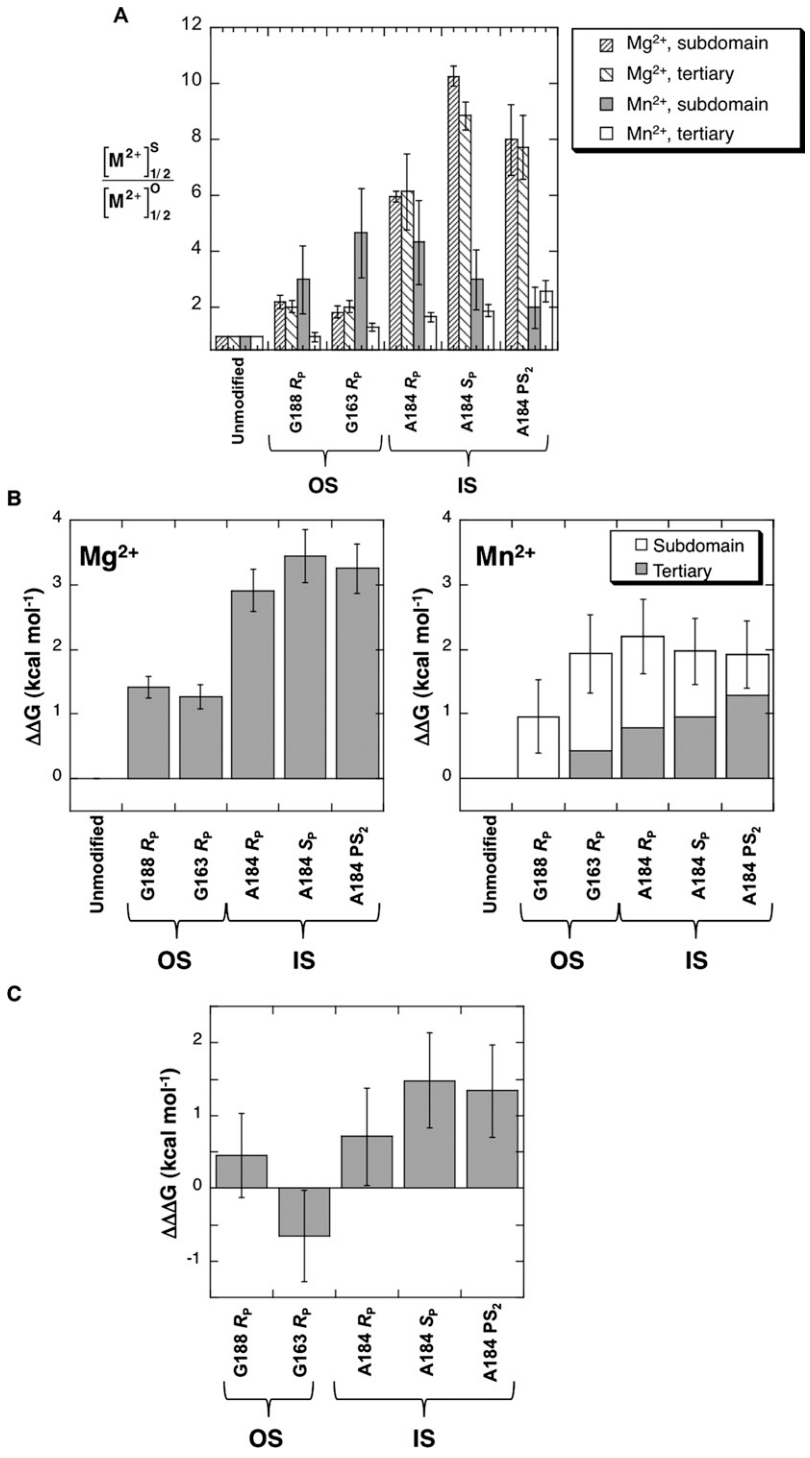

FIGURE 7. (*A*) Divalent metal-ion midpoint ratios of P4–P6 variants folded in either Mg^{2+} or Mn^{2+} in a background of 20 mM Na^+, separated into subdomain and tertiary folding midpoints (OS: outer-sphere metal-ion ligand; IS: inner-sphere metal-ion ligand). (*B*) Calculated ΔΔG values (relative to unmodified P4–P6) associated with Mg^{2+}-induced (*left*) and Mn^{2+}-induced (*right*) folding of P4–P6 phosphorothioate variants with respect to unmodified P4–P6. The values were calculated according to a thermodynamic framework in which the Hill coefficient is assumed to vary linearly with the divalent metal-ion concentration (model 2, Supplemental Material). The values for Mn^{2+} are arranged in a stacked plot that reflects the sum of the contributions from the separate U-to-I_{P5abc} (subdomain) and I_{P5abc}-to-F (tertiary) folding transitions. (*C*) Calculated ΔΔΔG values associated with Mg^{2+}- vs. Mn^{2+}-induced folding of phosphorothioate-substituted P4–P6 variants in a background of 20 mM Na^+.

apart in hammerhead ribozyme X-ray structures (Wang et al. 1999), and subsequent X-ray structures of more active forms of the hammerhead provided strong support for this proposed conformational transition and metal-ion binding site (Martick and Scott 2006; Nelson and Uhlenbeck 2006). Extensive studies of group I ribozyme catalysis provided evidence for three active site metal ions and multiple ligand interactions, with all but one of these interactions supported by X-ray structural studies (Shan et al. 1999; Guo et al. 2004; Golden et al. 2005; Stahley and Strobel 2005; Hougland et al. 2006). In this case the structural evidence for two metal ions remains to be resolved with the functional evidence for three metal ions; it is possible that this case presents a rare example of metal-ion recruitment upon thio substitution (Hougland et al. 2006).

The observation from a previous nucleotide analog interference mapping (NAIM) analysis that Mn^{2+} appeared to suppress P4–P6 folding defects caused by sulfur substitution at outer-sphere ligands challenged the "standard" interpretation of metal-ion rescue experiments (Basu and Strobel 1999). It was possible that the combination of sulfur substitution with Mn^{2+} supplanted outer-sphere interactions between Mg^{2+} and the phosphate oxygen with inner-sphere interactions between Mn^{2+} and sulfur, engendered by the longer sulfur–phosphorus bond coupled with the longer sulfur-Mn^{2+} coordination distance. Alternatively, the apparent rescue might have reflected limitations associated with the native gel assay of folding, the single rescuing conditions used, or the thermodynamic assumptions underlying the analysis of the results.

We first used simplifying conditions, investigating P4–P6 folding and rescue in a high background concentration of monovalent cation. We previously showed that these conditions essentially saturate the ion atmosphere with monovalent cations, thereby simplifying divalent metal-ion-dependent folding such that the observed Hill slope of two corresponds precisely to the uptake of two metal ions

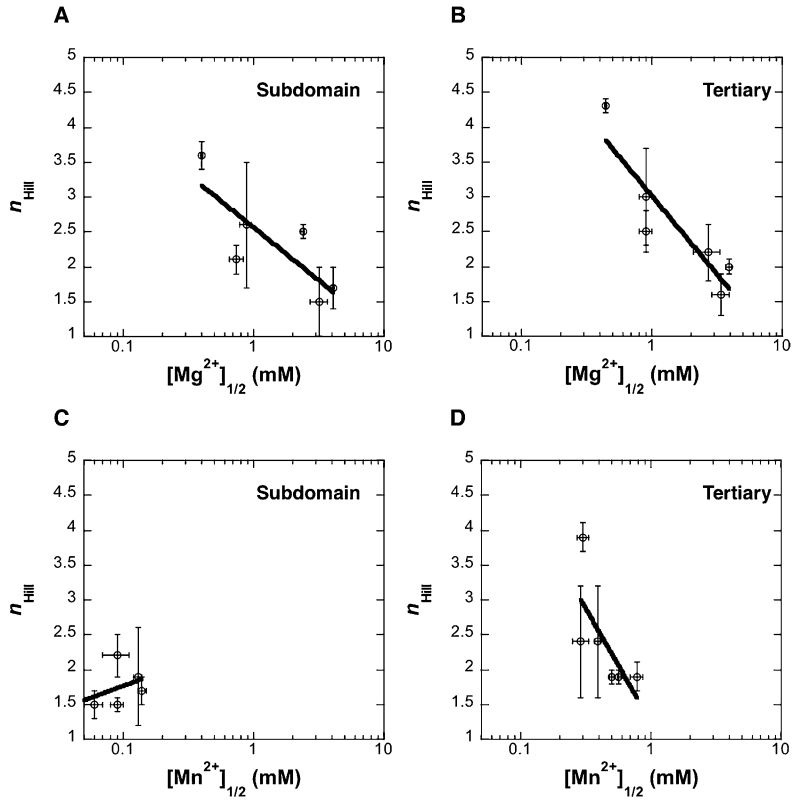

FIGURE 8. Linear fits to midpoint and Hill coefficient data according to model 2 (Equation 6) for folding of P4–P6 variants in Mg^{2+} (*A*,*B*) and in Mn^{2+} (*C*,*D*) in a background of 20 mM Na^{+}. (Data from Table 3.)

upon folding (Das et al. 2005b). At the time, we presumed that these two metal ions corresponded to site-bound metal ions in the P4–P6 crystallographic model, likely the most highly coordinated metal ions within the core of the P5abc domain (Fig. 1C, left). The rescue results here provide strong and direct support for this hypothesis and further reveal the identity of these metal ions.

While the simplifying high monovalent concentration conditions have been powerful for P4–P6 and for some other systems, not all RNAs will be as well behaved under these conditions, and it is desirable to also investigate RNAs under more physiologic conditions that allow more normal interactions with proteins and other binding partners. We also wished to investigate rescue under low-salt conditions to provide a more direct comparison to and test of the prior study that had called into question the ability of rescue experiments to discriminate between inner- and outer-sphere structural metal ions.

We found that the thermodynamic folding pathway differed in Mg^{2+} vs. Mn^{2+} in this low monovalent salt concentration background. In Mn^{2+}, we observed stabilization and accumulation of a folding intermediate corresponding to the P5abc subdomain of P4–P6 (I_{P5abc}), a structure that contains the two metal-ion binding sites identified above and has previously been shown to fold independently (Murphy and Cech 1993; Wu and Tinoco 1998; Silverman et al. 1999; Zheng et al. 2001). The presence of two different folding pathways subverts simple thermodynamic analysis of the rescue experiments and was a key element limiting the prior data interpretation. This limitation is akin to the potential to be misled in rescue experiments that probe catalysis when different reaction steps are followed or different rate-limiting steps occur for the constructs being compared (Shan and Herschlag 2000; Hougland et al. 2005). By obtaining residue-by-residue folding isotherms via hydroxyl radical footprinting (Fig. 6) and by developing an approach to compare folding free energies under common conditions, we were able to determine the thermodynamics for the overall folding process and to demonstrate rescue of inner-sphere, but not outer-sphere ligands. Our findings underscore the importance of developing explicit thermodynamic models and carrying out complete thermodynamic characterizations.

Our results show that metal-ion rescue experiments can be successfully applied to identify ligands of structural

TABLE 4. Folding free energy differences of unmodified vs. phosphorothioate-substituted P4–P6 in 20 mM Na^{+}

		ΔΔG (kcal mol^{-1})				
		Mg^{2+}	Mn^{2+}			
Construct	Ligand type	U→F	U→I_{P5abc}	I_{P5abc}→F	U→F	ΔΔΔG (U→F) (kcal mol^{-1})
G188 R_P	OS	1.41 ± 0.17	1.02 ± 0.47	−0.06 ± 0.30	0.96 ± 0.56	0.45 ± 0.58
G163 R_P	OS	1.27 ± 0.18	1.50 ± 0.57	0.43 ± 0.18	1.93 ± 0.60	−0.66 ± 0.63
A184 R_P	IS	2.91 ± 0.33	1.42 ± 0.55	0.78 ± 0.19	2.20 ± 0.58	0.71 ± 0.67
A184 S_P	IS	3.45 ± 0.41	1.02 ± 0.47	0.95 ± 0.21	1.97 ± 0.51	1.48 ± 0.65
A184 PS_2	IS	3.25 ± 0.38	0.62 ± 0.40	1.29 ± 0.32	1.91 ± 0.52	1.34 ± 0.64

metal ions, analogous to the use of rescue experiments to identify catalytic interactions of metal ions. As an increasing number of RNAs with biological roles other than catalysis are being identified, tools to dissect folding and metal ion and other interactions within folded structures will be increasingly important. Recent advances that increase the throughput and precision in analysis of nucleic acid footprinting data (Das et al. 2005a, 2010; Merino et al. 2005; Yoon et al. 2011), as well as the conceptual approaches introduced herein, should greatly facilitate analysis of these RNAs.

MATERIALS AND METHODS

Cloning

The plasmid pUC19 ΔC209 P4–P6 was a gift from Kara Juneau and Tom Cech and encodes full-length ΔC209 P4–P6 with a 5′ T7 promoter sequence, cloned between the EcoRI and XbaI restriction sites of the pUC19 vector. The plasmid pUC19 102-178 HH was a gift of Scott K. Silverman and encodes nucleotides 102–178 of P4–P6, followed by a hammerhead ribozyme cleavage sequence, cloned between the EcoRI and HindIII restriction sites of pUC19 (Silverman and Cech 1999). Two additional plasmids, pUC19 175-261 ΔC209 and pUC19 200-261 ΔC209, encoding T7 transcripts 175–261 and 200–261, respectively, of ΔC209 P4–P6 were constructed via PCR from pUC19 ΔC209 P4–P6. The PCR products for these constructs were cloned into pUC19 between the EcoRI and XbaI restriction sites. The sequences of all constructs were verified by forward and reverse automated sequencing.

RNA preparation

Linearization of all plasmids was accomplished by overnight digestion with EarI, except for pUC19 102–178 HH, which was linearized by overnight digestion with HindIII. Typical transcription reactions contained 40 mM Tris-HCl (pH 8), 25 mM $MgCl_2$, 2 mM spermidine, 0.01% Triton X-100, 4 mM NTPs, 10 mM DTT, 50 μg/mL linearized plasmid, 2 units/mL inorganic pyrophosphatase, and 84.6 μg/mL T7 RNA polymerase (prepared in the Piccirilli lab by Joseph Olvera). Transcription reactions of pUC19 102-178 HH included 30 mM $MgCl_2$ to ensure sufficient hammerhead ribozyme cleavage (Silverman and Cech 1999). Transcription reactions that used pUC19 175–261 ΔC209 or pUC19 200–261 ΔC209 included 10 mM GMP to ensure the presence of a 5′ monophosphate. All transcriptions were carried out at 37°C for 2 h. Transcripts were purified via 8% denaturing PAGE and electroeluted into TE pH 7.5, extracted with 25:25:1 (v/v/v) phenol/chloroform/isoamyl alcohol, precipitated with ethanol, and stored at –20°C.

RNA nucleotides 102–153 of ΔC209 P4–P6 were obtained by digestion of full-length ΔC209 P4–P6 RNA with the 10–23 DNAzyme 5′-AAGGCCATCTCAAAGGGCTAGCTACAACGATTCCCCTGAG ACTTG-3′, purchased from Integrated DNA Technologies (Santoro and Joyce 1997). About 16 nmol of ΔC209 P4–P6 RNA were combined with 25 nmol of DNAzyme, heated at 95°C for 3 min, and placed on ice for 1 min. Following the addition of 5x DNAzyme buffer (750 mM NaCl, 200 mM tris-HCl at pH 8), the mixture was incubated at 37°C for 30 min to allow hybridization. To initiate cleavage, $MgCl_2$ was added to a final concentration of 60 mM, and the reaction was allowed to proceed at 37°C for 5 h. The reaction was then treated with 25 units of RNase-free DNase (Promega) for 1 h at 37°C to remove the DNAzyme. Following phenol/chloroform/isoamyl alcohol extraction and ethanol precipitation, the desired 52-nt product was purified via 6% dPAGE.

As a result of 3′-end processing, the RNA molecules 102–178 and 102–153 contained 3′-terminal 2′,3′-cyclic phosphate groups. To remove these groups, the RNAs were treated with T4 polynucleotide kinase (T4 PNK; New England Biolabs) based on a protocol described previously (Silverman and Cech 1999). Briefly, ~5–10 nmol of RNA were incubated with 50–100 units of T4 PNK in 1x kinase buffer (50 mM tris-HCl at pH 7.5, 10 mM $MgCl_2$, 5 mM DTT) at 37°C for 5 h. The RNAs were then extracted with phenol/chloroform/isoamyl alcohol and precipitated with ethanol.

Synthetic monophosphorothioate RNA oligonucleotides 179–199 A184 PS and 154–174 G163 PS of ΔC209 P4–P6 were purchased from Dharmacon, Inc. Phosphorothioate diastereomers were separated via anion exchange HPLC (Frederiksen and Piccirilli 2009). The RNA oligonucleotide 179–199 containing a phosphorodithioate linkage 5′ of nucleotide A184 was synthesized on a 1-μmol scale on an Expedite 8909 nucleic acid synthesizer. Except at position 183, this oligo was synthesized with standard RNA phosphoramidites. At position 183, an adenosine phosphorothioamidite was coupled that had been synthesized based on methods described previously (Petersen and Nielsen 1990). Following a 30-min coupling or double coupling step, the initial dichlorobenzyl phosphorothioate linkage was converted to a phosphorodithioate linkage by a 400-sec oxidation with 5% sulfur in 1:1 (v/v) pyridine/carbon disulfide or with 0.05 M solution of sulfurizing reagent II in 2:3 (v/v) pyridine/acetonitrile. After synthesis of the full-length oligo had been completed, the dichlorobenzyl protecting group was removed by treatment with 1:1:2 (v/v/v) thiophenol/triethylamine/dioxane at room temperature for 2 h. The solid support was then washed three times each with methanol and diethyl ether and allowed to dry. Base deprotection and cleavage from the solid support was achieved by treatment with 3:1 (v/v) ammonium hydroxide/ethanol for 2 h at 55°C. Following evaporation of the ethanolic ammonia solution, the 2′-silyl protecting groups were removed by treatment with a 6:3:4 (v/v/v) solution of *N*-methyl pyrrolidinone/triethylamine/triethylamine trihydrofluoride at 65°C for 1.5 h (Wincott et al. 1995). The deprotected phosphorodithioate oligonucleotide was then purified by anion-exchange HPLC and could be clearly distinguished from the R_P and S_P monothioate species, which elute earlier from the column than the dithioate. The mass of the phosphorodithioate oligo was confirmed by MALDI mass spectrometry (calculated for M-H: 6787.9, measured 6787.1).

Modified P4–P6 RNAs prepared by splint ligation

Schemes describing construction of phosphorothioate-modified RNAs are shown in Supplemental Figure S1. When possible, synthetic phosphorothioate oligonucleotides were ordered with 5′-phosphate groups (Dharmacon). The phosphorodithioate oligo was phosphorylated on its 5′ end by using T4 PNK and ATP. RNAs were joined by using standard DNA splint ligation methods (Moore and Sharp 1992). In a typical reaction, 5 nmol of each component (splint, 5′ RNA and 3′ RNA) were combined in TE pH 7.5 (10 mM tris-HCl at pH 7.5, 1 mM Na_2EDTA pH 8),

heated to 90°C for 4 min, placed on ice for 1 min, and incubated at 37°C for 30 min. To this mixture were added 10x ligation buffer, 500 pmol T4 DNA ligase (prepared in the Piccirilli lab by Joseph Olvera) and water so that the final volume was as small as possible while still keeping the final concentration of glycerol below 5%. Beside RNA, splint, and T4 DNA ligase, the final ligation reaction contained 40 mM tris-HCl (pH 7.5), 10 mM $MgCl_2$, 10 mM DTT, 1 mM ATP, and 0.05 mg/mL bovine serum albumin. Ligation reactions were allowed to proceed for 4–5 h at 37°C, after which time the DNA splint was removed by treatment with RQ1 RNase-free DNase (Promega, Inc.). Following phenol/chloroform/isoamyl alcohol extraction and ethanol precipitation, the ligation products were purified via 6% dPAGE and subsequent electroelution into TE pH 7.5. Ligation junctions were confirmed by alkaline hydrolysis and T1 ladders, while iodine cleavage was used to confirm the positions of the phosphorothioate linkages.

Fe-EDTA footprinting

Full-length ΔC209 P4–P6 molecules were 5′-end labeled by treatment with [γ-^{32}P]ATP and T4 PNK, gel purified by 6% dPAGE, eluted passively overnight into TE pH 7.5 at 4°C, extracted with phenol/chloroform/isoamyl alcohol, and precipitated with ethanol. Prior to storage at –20°C, labeled RNAs were resuspended in water to an activity of ~100,000 cpm/μL to minimize autoradiolysis.

A mix was prepared and distributed in 8-μL aliquots so that each footprinting reaction initially contained 1 μL of 5′-end labeled RNA, 1 μL of 500 mM Na-MOPS (pH 7), and 6 μL of water. Reactions carried out in the presence of 2 M NaCl contained 4 μL of 5 M NaCl and 2 μL of water. Following the addition of 1 μL of a 10x solution of $MgCl_2$ or $MnCl_2$, the RNA was allowed to fold for ~15 min at room temperature.

A 10x footprinting reagent was prepared separately that contained 1 mM $Fe(NH_4)_2(SO_4)_2$, 1.25 mM EDTA (pH 8), and 60 mM sodium ascorbate. To initiate the footprinting reaction, 1 μL of this reagent was added to each aliquot to a final volume of 10 μL so that each reaction contained labeled RNA, 50 mM Na-MOPS (pH 7), 2 M NaCl where appropriate, varying concentrations of $MgCl_2$ or $MnCl_2$, 0.1 mM $Fe(NH_4)_2(SO_4)_2$, 0.125 mM EDTA (pH 8), and 6 mM sodium ascorbate. The reaction was allowed to proceed for 30 min at room temperature, and was quenched by the addition of 5 μL of a thiourea stop solution (9 M urea, 300 mM thiourea, 0.1% each xylene cyanol and bromophenol blue).

The footprinting reactions (7 μL of each) were fractionated on 8%–8.5% denaturing gels. The gels were dried, exposed to storage phosphor screens, and scanned on a Typhoon Trio imager (GE Healthcare). Gels were quantified using the SAFA program (Das et al. 2005a). Importantly, for residues that become protected only upon addition of divalent metal ions, no significant difference in cleavage intensity was found between samples folded in 2 M NaCl alone and samples folded in 20 mM Na^+ alone. This result argues against a significant effect of contaminating divalent metal ions in the 2 M NaCl samples.

Initial data analysis and curve fitting

Regions of protection from hydroxyl radical cleavage were identified as follows. Footprinting in 2 M NaCl yielded clear divalent metal-ion-dependent protections at nucleotides 164, 176–177, 180–182, and 187, corresponding to folding of the P5abc subdomain. In 20 mM Na^+, protections at nucleotides 152–153 and 200–202, and at 176–177 and 180–182, were chosen to reflect tertiary and subdomain folding, respectively. At each nucleotide position, each individual footprinting experiment generated a set of intensities whose values decreased in proportion to the extent of protection. The intensity data were fit initially to a four-parameter Hill equation as described in the Supplemental Material (Equation S1) and were subsequently normalized based on these fits. Data for protected regions spanning multiple nucleotides (e.g., 152–153 or 180–182) were averaged for each experiment. All of the data corresponding to a given folding transition derived from two to four independent experiments per RNA construct were then plotted on the same graph. For example, each plot in Figure 3 contains all data associated with nucleotides 164, 176–177, 180–182, and 187 (when available) obtained from each footprinting experiment conducted in 2 M NaCl. We then took the average of all of the protection data at each divalent metal-ion concentration and fit the resulting points to the Hill equation to produce the final curves shown in Figures 3 and 6. The midpoints and Hill coefficients derived from these curves were then used to determine ΔΔG and ΔΔΔG values for the constructs according to procedures outlined in the Supplemental Material. Finally, an independent analysis based on a rigorous likelihood formalism was carried out and gave indistinguishable results for the thermodynamic parameters and their errors (see Supplemental Material, Supplemental Figs. S3–S5, and Supplemental Tables S3, S4).

SUPPLEMENTAL MATERIAL

Supplemental material is available for this article.

ACKNOWLEDGMENTS

We thank Kara Juneau, Tom Cech, and Scott Silverman for gifts of reagents and Joseph Olvera for technical assistance. We also thank Dr. Tobin Sosnick, Dr. Jonathan Staley, and Dr. Carl Correll for helpful discussions, and members of the Piccirilli lab for comments on the manuscript. This work was supported by NIH grants to D.H. (GM 49243) and J.A.P. (GM 088656), and by a Jane Coffin Childs Foundation Fellowship (to R.D.). J.K.F. was also supported by the University of Chicago Medical Scientist Training Program (5 T32 GM07281).

Received June 14, 2011; accepted January 17, 2012.

REFERENCES

Adams PL, Stahley MR, Kosek AB, Wang JM, Strobel SA. 2004. Crystal structure of a self-splicing group I intron with both exons. *Nature* **430:** 45–50.

Anderson CF, Record MT Jr. 1990. Ion distributions around DNA and other cylindrical polyions: theoretical descriptions and physical implications. *Annu Rev Biophys Biophys Chem* **19:** 423–465.

Bai Y, Greenfeld M, Travers KJ, Chu VB, Lipfert J, Doniach S, Herschlag D. 2007. Quantitative and comprehensive decomposition of the ion atmosphere around nucleic acids. *J Am Chem Soc* **129:** 14981–14988.

Basu S, Strobel SA. 1999. Thiophilic metal ion rescue of phosphorothioate interference within the *Tetrahymena* ribozyme P4–P6 domain. *RNA* **5:** 1399–1407.

Bukhman YV, Draper DE. 1997. Affinities and selectivities of divalent cation binding sites within an RNA tertiary structure. *J Mol Biol* **273:** 1020–1031.

Cate JH, Gooding AR, Podell E, Zhou KH, Golden BL, Kundrot CE, Cech TR, Doudna JA. 1996. Crystal structure of a group I ribozyme domain: Principles of RNA packing. *Science* **273:** 1678–1685.

Cate JH, Hanna RL, Doudna JA. 1997. A magnesium ion core at the heart of a ribozyme domain. *Nat Struct Biol* **4:** 553–558.

Chen Y, Li X, Gegenheimer P. 1997. Ribonuclease P catalysis requires Mg^{2+} coordinated to the *pro-*R_P oxygen of the scissile bond. *Biochemistry* **36:** 2425–2438.

Christian EL. 2005. Identification and characterization of metal ion binding by thiophilic metal ion rescue. In *Handbook of RNA biochemistry* (ed. RK Hartmann). Wiley-VCH Verlag GmbH & Co., Weinheim, Germany.

Chu VB, Bai Y, Lipfert J, Herschlag D, Doniach S. 2008. A repulsive field: advances in the electrostatics of the ion atmosphere. *Curr Opin Chem Biol* **12:** 619–625.

Costa FF. 2010. Non-coding RNAs: Meet thy masters. *Bioessays* **32:** 599–608.

Darby MK, Trayer IP. 1983. Metal-nucleotide structure at the active sites of the mammalian hexokinases. *Eur J Biochem* **129:** 555–560.

Das R, Laederach A, Pearlman SM, Herschlag D, Altman RB. 2005a. SAFA: Semi-automated footprinting analysis software for high-throughput quantification of nucleic acid footprinting experiments. *RNA* **11:** 344–354.

Das R, Travers KJ, Bai Y, Herschlag D. 2005b. Determining the Mg^{2+} stoichiometry for folding an RNA metal ion core. *J Am Chem Soc* **127:** 8272–8273.

Das R, Karanicolas J, Baker D. 2010. Atomic accuracy in predicting and designing noncanonical RNA structure. *Nat Methods* **7:** 291–294.

Draper DE, Grilley D, Soto AM. 2005. Ions and RNA folding. *Annu Rev Biophys Biomol Struct* **34:** 221–243.

Fang X, Pan T, Sosnick TR. 1999. A thermodynamic framework and cooperativity in the tertiary folding of a Mg^{2+}-dependent ribozyme. *Biochemistry* **38:** 16840–16846.

Forconi M, Herschlag D. 2009. Use of phosphorothioates to identify sites of metal-ion binding in RNA. *Methods Enzymol* **468:** 311–333.

Forconi M, Lee J, Lee JK, Piccirilli JA, Herschlag D. 2008. Functional identification of ligands for a catalytic metal ion in group I introns. *Biochemistry* **47:** 6883–6894.

Frederiksen JK, Piccirilli JA. 2009. Separation of RNA phosphorothioate oligonucleotides by HPLC. *Meth Enzymol* **468:** 289–309.

Garcia HG, Kondev J, Orme N, Theriot JA, Phillips R. 2011. Thermodynamics of biological processes. *Methods Enzymol* **492:** 27–59.

Golden BL, Kim H, Chase E. 2005. Crystal structure of a phage *Twort* group I ribozyme-product complex. *Nat Struct Mol Biol* **12:** 82–89.

Gordon PM, Fong R, Piccirilli JA. 2007. A second divalent metal ion in the group II intron reaction center. *Chem Biol* **14:** 607–612.

Guo F, Gooding AR, Cech TR. 2004. Structure of the *Tetrahymena* ribozyme: Base triple sandwich and metal ion at the active site. *Mol Cell* **16:** 351–362.

Horton TE, Clardy DR, DeRose VJ. 1998. Electron paramagnetic resonance spectroscopic measurement of Mn^{2+} binding affinities to the hammerhead ribozyme and correlation with cleavage activity. *Biochemistry* **37:** 18094–18101.

Hougland JL, Kravchuk AV, Herschlag D, Piccirilli JA. 2005. Functional identification of catalytic metal ion binding sites within RNA. *PLoS Biol* **3:** 1536–1548.

Hougland JL, Piccirilli JA, Forconi M, Lee J, Herschlag D. 2006. How the group I intron works: A case study of RNA structure and function. In *The RNA world: The nature of modern RNA suggests a prebiotic RNA world*, 3rd edition (ed. RF Gesteland et al.). Cold Spring Harbor Laboratory Press, Cold Spring Harbor, NY.

Jaffe EK, Cohn M. 1978. Divalent cation-dependent stereospecificity of adenosine 5′-*O*-(2-thiotriphosphate) in the hexokinase and pyruvate kinase reactions. The absolute stereochemistry of the diastereoisomers of adenosine 5′-*O*-(2-thiotriphosphate). *J Biol Chem* **253:** 4823–4825.

Juneau K, Cech TR. 1999. In vitro selection of RNAs with increased tertiary structure stability. *RNA* **5:** 1119–1129.

Juneau K, Podell E, Harrington DJ, Cech TR. 2001. Structural basis of the enhanced stability of a mutant ribozyme domain and a detailed view of RNA-solvent interactions. *Structure* **9:** 221–231.

Lee CS, O'Sullivan WJ. 1985. The interaction of phosphorothioate analogues of ATP with phosphomevalonate kinase. Kinetic and ^{31}P NMR studies. *J Biol Chem* **260:** 13909–13915.

Leipply D, Draper DE. 2010. Dependence of RNA tertiary structural stability on Mg^{2+} concentration: interpretation of the Hill equation and coefficient. *Biochemistry* **49:** 1843–1853.

Leipply D, Lambert D, Draper DE. 2009. Ion-RNA interactions thermodynamic analysis of the effects of mono- and divalent ions on RNA conformational equilibria. *Methods Enzymol* **469:** 433–463.

Manning GS. 1977a. Limiting laws and counterion condensation in polyelectrolyte solutions. IV. The approach to the limit and the extraordinary stability of the charge fraction. *Biophys Chem* **7:** 95–102.

Manning GS. 1977b. Theory of the delocalized binding of Mg(II) to DNA: preliminary analysis for low binding levels. *Biophys Chem* **7:** 141–145.

Manning GS. 1978. Limiting laws and counterion condensation in polyelectrolyte solutions. V. Further development of the chemical model. *Biophys Chem* **9:** 65–70.

Martick M, Scott WG. 2006. Tertiary contacts distant from the active site prime a ribozyme for catalysis. *Cell* **126:** 309–320.

Merino EJ, Wilkinson KA, Coughlan JL, Weeks KM. 2005. RNA structure analysis at single nucleotide resolution by selective 2′-hydroxyl acylation and primer extension (SHAPE). *J Am Chem Soc* **127:** 4223–4231.

Misra VK, Draper DE. 1998. On the role of magnesium ions in RNA stability. *Biopolymers* **48:** 113–135.

Moore MJ, Sharp PA. 1992. Site-specific modification of pre-RNA: the 2′-hydroxyl groups at the splice sites. *Science* **256:** 992–997.

Murphy FL, Cech TR. 1993. An independently folding domain of RNA tertiary structure within the *Tetrahymena* ribozyme. *Biochemistry* **32:** 5291–5300.

Murphy FL, Cech TR. 1994. GAAA tetraloop and conserved bulge stabilize tertiary structure of a group I intron domain. *J Mol Biol* **236:** 49–63.

Nelson JA, Uhlenbeck OC. 2006. When to believe what you see. *Mol Cell* **23:** 447–450.

Pecoraro VL, Rendina AR, Cleland WW. 1985. Determination of the screw sense specificity of bovine liver fructokinase. *Biochemistry* **24:** 1619–1622.

Petersen KH, Nielsen J. 1990. Chemical synthesis of dimer ribonucleotides containing internucleotidic phosphorodithioate linkages. *Tetrahedron Lett* **31:** 911–914.

Piccirilli JA, Vyle JS, Caruthers MH, Cech TR. 1993. Metal-ion catalysis in the *Tetrahymena* ribozyme reaction. *Nature* **361:** 85–88.

Rook MS, Treiber DK, Williamson JR. 1999. An optimal Mg^{2+} concentration for kinetic folding of the *Tetrahymena* ribozyme. *Proc Natl Acad Sci* **96:** 12471–12476.

Santoro SW, Joyce GF. 1997. A general purpose RNA-cleaving DNA enzyme. *Proc Natl Acad Sci* **94:** 4262–4266.

Schwans JP, Cortez CN, Olvera JM, Piccirilli JA. 2003. 2′-mercaptonucleotide interference reveals regions of close packing within folded RNA molecules. *J Am Chem Soc* **125:** 10012–10018.

Shan SO, Herschlag D. 2000. An unconventional origin of metal-ion rescue and inhibition in the *Tetrahymena* group I ribozyme reaction. *RNA* **6:** 795–813.

Shan SO, Yoshida A, Sun SG, Piccirilli JA, Herschlag D. 1999. Three metal ions at the active site of the *Tetrahymena* group I ribozyme. *Proc Natl Acad Sci* **96:** 12299–12304.

Silverman SK, Cech TR. 1999. Energetics and cooperativity of tertiary hydrogen bonds in RNA structure. *Biochemistry* **38:** 8691–8702.

Silverman SK, Zheng MX, Wu M, Tinoco I, Cech TR. 1999. Quantifying the energetic interplay of RNA tertiary and secondary structure interactions. *RNA* **5:** 1665–1674.

Sontheimer EJ, Sun S, Piccirilli JA. 1997. Metal ion catalysis during splicing of premessenger RNA. *Nature* **388:** 801–805.

Stahley MR, Strobel SA. 2005. Structural evidence for a two-metal-ion mechanism of group I intron splicing. *Science* **309:** 1587–1590.

Takamoto K, Das R, He Q, Doniach S, Brenowitz M, Herschlag D, Chance MR. 2004. Principles of RNA compaction: Insights from the equilibrium folding pathway of the P4-P6 RNA domain in monovalent cations. *J Mol Biol* **343:** 1195–1206.

Travers KJ, Boyd N, Herschlag D. 2007. Low specificity of metal ion binding in the metal ion core of a folded RNA. *RNA* **13:** 1205–1213.

Wang S, Karbstein K, Peracchi A, Beigelman L, Herschlag D. 1999. Identification of the hammerhead ribozyme metal ion binding site responsible for rescue of the deleterious effect of a cleavage site phosphorothioate. *Biochemistry* **38:** 14363–14378.

Weinstein LB, Jones BC, Cosstick R, Cech TR. 1997. A second catalytic metal ion in group I ribozyme. *Nature* **388:** 805–808.

Weiss JN. 1997. The Hill equation revisited: uses and misuses. *FASEB J* **11:** 835–841.

Wincott F, DiRenzo A, Shaffer C, Grimm S, Tracz D, Workman C, Sweedler D, Gonzalez C, Scaringe S, Usman N. 1995. Synthesis, deprotection, analysis and purification of RNA and ribozymes. *Nucleic Acids Res* **23:** 2677–2684.

Wu M, Tinoco I Jr. 1998. RNA folding causes secondary structure rearrangement. *Proc Natl Acad Sci* **95:** 11555–11560.

Yoon S, Kim J, Hum J, Kim H, Park S, Kladwang W, Das R. 2011. HiTRACE: high-throughput robust analysis for capillary electrophoresis. *Bioinformatics* **27:** 1798–1805.

Yoshida A, Sun SG, Piccirilli JA. 1999. A new metal ion interaction in the *Tetrahymena* ribozyme reaction revealed by double sulfur substitution. *Nat Struct Biol* **6:** 318–321.

Zheng M, Wu M, Tinoco I Jr. 2001. Formation of a GNRA tetraloop in P5abc can disrupt an interdomain interaction in the *Tetrahymena* group I ribozyme. *Proc Natl Acad Sci* **98:** 3695–3700.

SUPPLEMENTAL MATERIAL

Evaluation of folding midpoints and Hill coefficients for divalent ion titrations

Hydroxyl radical footprinting data *d* summed over a subset of nucleotides (e.g., 180, 181, & 182) were fit to Hill isotherms by least-squares optimization in KaleidaGraph:

$$d = A + B\frac{\left(\frac{[M^{2+}]}{[M^{2+}]_{1/2}}\right)^n}{1+\left(\frac{[M^{2+}]}{[M^{2+}]_{1/2}}\right)^n} \qquad \text{(S1)}$$

Each fit returned four parameters – the "unfolded" reactivity *A,* the maximal change in reactivity *B*, the midpoint $[M^{2+}]_{1/2}$, and the apparent Hill coefficient *n* – along with their associated errors δA, δB, $\delta[M^{2+}]_{1/2}$, and δn. Independently fitted values for multiple subsets of residues (e.g., 176-177 and 180-182) were averaged, with appropriate weighting and assuming normally distributed errors, to yield the final values of $[M^{2+}]_{1/2}$ and *n* for each individual folding transition. Explicitly, given midpoints $\left([M^{2+}]_{1/2}\right)_i \pm \delta\left([M^{2+}]_{1/2}\right)_i$ obtained for data over different residue subsets *i*, the averaged midpoints and associated errors were calculated as:

$$[M^{2+}]_{1/2} = \frac{\sum_i \frac{\left([M^{2+}]_{1/2}\right)_i}{\delta\left([M^{2+}]_{1/2}\right)_i^2}}{\sum_i \frac{1}{\delta\left([M^{2+}]_{1/2}\right)_i^2}} \qquad \text{(S2)}$$

$$\delta[M^{2+}]_{1/2} = \left[\sum_i \frac{1}{\delta\left([M^{2+}]_{1/2}\right)_i^2}\right]^{-1/2} \qquad \text{(S3)}$$

An analogous relation was used to average the apparent Hill coefficients and obtain their associated errors.

Derivation of thermodynamic relations for models with non-constant Hill coefficients

Model 1. Two site-bound metal ions, derived from solution or from the atmosphere.

We derive the free energy relations and apparent Hill coefficients (Weiss 1997; Garcia et al. 2011) for the following model of the P4-P6 folding transition in a background of 2 M NaCl:

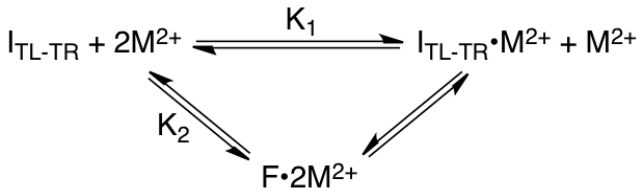

For simplicity, this scheme does not show additional diffusely associated 'background' divalent metal ions, which are assumed to be equal in number for each species. The scheme also does not show monovalent ions (Na^+ herein), since we are considering the dependence of folding on the divalent metal ion concentration only. Finally, the scheme neglects anions, since the divalent ion titrations minimally perturb the solution concentration of anions in the presence of 2 M NaCl. The Boltzmann weights for each state sum to the partition function for the system:

$$Z = P_1 + P_2 + P_3 = 1 + \frac{[M^{2+}]}{K_1} + \left(\frac{[M^{2+}]}{K_2}\right)^2 \qquad \text{(S4)}$$

Here, K_1 parameterizes the equilibrium between the first and second states (for associating a single divalent metal ion with the $I_{TL/TR}$ state), and K_2 parameterizes the equilibrium for folding between the first state and the third state. The free energy difference between the two $I_{TL/TR}$ states and F is then:

$$\Delta G = -RT \ln\left[\frac{P_3}{(P_1 + P_2)}\right] = -RT \ln\left[\frac{\left(\frac{[M^{2+}]}{K_2}\right)^2}{1 + \left(\frac{[M^{2+}]}{K_1}\right)}\right] \qquad \text{(S5)}$$

The apparent Hill coefficient is defined by the thermodynamic relation:

$$n = -\frac{1}{RT}\frac{\partial \Delta G}{\partial \ln[M^{2+}]} \qquad \text{(S6)}$$

Using equation S5 gives:

$$n = 2 - \frac{\left(\frac{[M^{2+}]}{K_1}\right)}{1+\left(\frac{[M^{2+}]}{K_1}\right)} \qquad \text{(S7)}$$

The fraction folded is given by:

$$f = \frac{P_3}{Z} = \frac{\left(\frac{[M^{2+}]}{K_2}\right)^2}{1+\left(\frac{[M^{2+}]}{K_1}\right)+\left(\frac{[M^{2+}]}{K_2}\right)^2} \qquad \text{(S8)}$$

At the folding midpoint $[M^{2+}]_{1/2}$, where by definition $\frac{P_3}{P_1+P_2}=1$, the following relation holds (setting equation S8 equal to 0.5):

$$K_2 = [M^{2+}]_{1/2}\left(1+\frac{[M^{2+}]_{1/2}}{K_1}\right)^{-1/2} \qquad \text{(S9)}$$

Equation S10 below can be derived by taking a Taylor expansion of $\ln[f/(1-f)]$ in equation S8 with respect to $\ln[M^{2+}]$ around the midpoint $[M^{2+}]_{1/2}$, and is a good approximation near the folding midpoint up to corrections logarithmic in $[M^{2+}]$.

$$f = \frac{\left(\frac{[M^{2+}]}{[M^{2+}]_{1/2}}\right)^{n\left([M^{2+}]_{1/2}\right)}}{1+\left(\frac{[M^{2+}]}{[M^{2+}]_{1/2}}\right)^{n\left([M^{2+}]_{1/2}\right)}} \qquad \text{(S10)}$$

Using $n\left([M^{2+}]_{1/2}\right)$ given by equation S7, we can evaluate equation S10 at the midpoint to give:

$$n\left([M^{2+}]_{1/2}\right) = 2 - \frac{[M^{2+}]_{1/2}}{K_1+[M^{2+}]_{1/2}} \qquad \text{(S11)}$$

Indeed, equation S10 is the standard Hill form used for least-squares fits (see equation S1) to estimate n_j and $\left([M^{2+}]_{1/2}\right)_j$, and associated errors δn_j and $\delta\left([M^{2+}]_{1/2}\right)_j$, for each RNA variant *j*. These values were then fit to equation S11 by χ^2 minimization (KaleidaGraph) to give the

parameter K_1 with standard errors δK_1, as shown in main text Figure 5. Finally, for comparing each modified variant to the wild type RNA, the midpoints were substituted into equation S5; applying equation S9 gives

$$\Delta\Delta G_j = 2RT \ln\left[\frac{\left([M^{2+}]_{1/2}\right)_j}{\left([M^{2+}]_{1/2}\right)_0}\right] - RT \ln\left[\frac{1+\frac{\left([M^{2+}]_{1/2}\right)_j}{K_1}}{1+\frac{\left([M^{2+}]_{1/2}\right)_0}{K_1}}\right] \qquad \text{(S12a)}$$

$$= 2RT \ln\left[\frac{\left(K_2\right)_j}{\left(K_2\right)_0}\right] \qquad \text{(S12b)}$$

where $\left([M^{2+}]_{1/2}\right)_0$ denotes the folding midpoint of the unmodified RNA, and $(K_2)_0$ and $(K_2)_j$ are the K_2 parameters fitted for the unmodified and variant RNAs, respectively. Note that, as desired, this expression is independent of the divalent ion concentration at which the free energy difference between the unmodified and modified RNAs is evaluated. The error on $\Delta\Delta G_j$ was dominated by uncertainty in K_1; it was evaluated by recalculating $\Delta\Delta G_j$ with $K_1 \pm \delta K_1$.

Model 2. Linear expansion of the apparent Hill coefficient.

This model makes no assumptions about the structural ensembles or their associated ion atmospheres and site-bound ions, although we continue to assume that the apparent Hill coefficient for all variants is the same at a given metal ion concentration $[M^{2+}]$ (but varies across metal ion concentrations). This model assumes that the apparent Hill coefficient can be expanded as a linear function of the logarithm of the divalent ion concentration, as is commonly seen in calculations as well as empirical fits to RNA folding isotherms. Explicitly, we write the expansion near the folding midpoint $\left(\left[M^{2+}\right]_{1/2}\right)_0$ of the unmodified RNA:

$$n_{\text{Hill}}\left(\left[M^{2+}\right]\right) = n_0 + \alpha_n \ln\left(\frac{\left[M^{2+}\right]}{\left(\left[M^{2+}\right]_{1/2}\right)_0}\right) \qquad \text{(S13)}$$

Here, n_0 is the apparent Hill coefficient of the unmodified RNA near its midpoint. For simplification, we let $\gamma = \frac{\left[M^{2+}\right]}{\left(\left[M^{2+}\right]_{1/2}\right)_0}$, the ratio of the metal ion concentration to the folding midpoint of the unmodified RNA. Then equation S13 becomes:

$$n_{\text{Hill}}\left(\left[M^{2+}\right]\right) = n_0 + \alpha_n \ln\gamma \tag{S14}$$

Integrating equation S6 gives the free energy for any variant *j* as:

$$\Delta G_j(\gamma) = -n_0 RT \ln\gamma - \frac{1}{2}\alpha_n RT(\ln\gamma)^2 + const \tag{S15}$$

The constant of integration (*const*) is readily determined by evaluating equation S15 at the folding midpoint of the unmodified RNA (γ = 1), where the free energy of a mutant is equal to $\Delta\Delta G_j$:

$$\Delta G_j(\gamma) = -n_0 RT \ln\gamma - \frac{1}{2}\alpha_n RT(\ln\gamma)^2 + \Delta\Delta G_j \tag{S16}$$

Finally, setting this expression equal to zero corresponds to evaluating $\Delta G_j(\gamma)$ at the folding midpoint $\left([M^{2+}]_{1/2}\right)_j$ of the modified variant *j*:

$$\Delta\Delta G_j = n_0 RT \ln\left[\frac{\left([M^{2+}]_{1/2}\right)_j}{\left([M^{2+}]_{1/2}\right)_0}\right]\left(n_0 + \frac{1}{2}\ln\left[\frac{\left([M^{2+}]_{1/2}\right)_j}{\left([M^{2+}]_{1/2}\right)_0}\right]\right) \tag{S17}$$

Noting that the apparent Hill coefficient for the mutant at its midpoint is $n_j = n_0 + \ln\left[\frac{\left([M^{2+}]_{1/2}\right)_j}{\left([M^{2+}]_{1/2}\right)_0}\right]$ gives a compact expression for the free energy difference $\Delta\Delta G_j$ associated with the modification:

$$\Delta\Delta G_j = \frac{n_0 + n_j}{2} RT \ln\left[\frac{\left([M^{2+}]_{1/2}\right)_j}{\left([M^{2+}]_{1/2}\right)_0}\right] \tag{S18}$$

In practice, we carried out independent least-squares Hill fits (see equation S1) to titrations for the unmodified and modified variants to yield n_j and $\left([M^{2+}]_{1/2}\right)_j$. Using equation S13, we then

carried out a least-squared fit to obtain n_0 and α_n, and their associated errors δn_0 and $\delta\alpha_n$. The midpoint values $\left([M^{2+}]_{1/2}\right)_j$ and the best-fit parameters for n_j (equation S13) were then substituted into equation S18 to give $\Delta\Delta G_j$ values. The error on $\Delta\Delta G_j$ was dominated by uncertainties in n_0 and α_n, and was estimated by recalculating $\Delta\Delta G_j$ with $n_0 \pm \delta n_0$ and $\alpha_n \pm \delta\alpha_n$, and summing the observed deviations in quadrature.

Calculation of P values

Values for $\Delta\Delta\Delta G$ were calculated by subtracting the $\Delta\Delta G$ obtained for Mn^{2+}-induced folding from that obtained for Mg^{2+}-induced folding. The associated *P* values were calculated using the Gauss error function (erf) in Microsoft Excel, according to

$$P = \frac{1 - \mathrm{erf}\left(\frac{\Delta\Delta\Delta G}{\delta\Delta\Delta\Delta G\sqrt{2}}\right)}{2} \qquad \text{(S19)}$$

where $\delta\Delta\Delta\Delta G$ is the standard error of $\Delta\Delta\Delta G$.

Complete likelihood-based inference of metal ion rescue from footprinting gels

The analysis given above permits the inference of $\Delta\Delta G$ and $\Delta\Delta\Delta G$ values, as well as their errors, for metal ion rescue experiments using common tools (Excel & KaleidaGraph), but makes assumptions about the Gaussianity of the errors to propagate the errors. Consequently, we have also carried out a complete likelihood-based analysis of the data without invoking such assumptions, using MATLAB scripts. This analysis gives consistent results. For completeness, we describe this analysis herein, presenting detailed equations for the high salt (2 M NaCl background) conditions.

Likelihood form

We make the following assumptions for computing the likelihood that the cleavage intensities read from a footprinting gel are consistent with a thermodynamic model:

1. The folding is a two-state process, as described, for example, in equation S8. The cleavage patterns of the unfolded and folded states are not known *a priori* but are to be estimated through the likelihood analysis.
2. The amount of sample loaded in each lane varies due to pipetting errors. The exact amount of this lane loading variation is a number to be estimated on a gel-by-gel basis.
3. Further deviations of peak intensities from the prediction are due to statistical errors (shot noise), random errors in the SAFA analysis procedure, nuclease contaminants, and variations in background cleavage. The latter issues in particular can affect residues in somewhat unpredictable ways. We assume that the range of deviations differs for each residue and needs to be estimated through the likelihood analysis. (For residues with large nuclease contaminants or background cleavage, we would hope that the analysis recognizes the large deviations from the model favored by the majority of residues and effectively downweights the contributions of anomalous residues.)
4. We assume that the error at each residue is *at least* 10% of the mean cleavage intensity. Allowing the likelihood fits to assume smaller errors appears to lead to overfitting, in which some residues are assigned too much confidence.

   Mathematically, the likelihood model is given by

$$L \propto \prod_{i,j} \frac{1}{\sigma_j} \exp\left[\frac{-\left(\alpha_i \left(C_j^{\text{unfold}} + \Delta C_j f_i^{\text{fold}} \right) - \text{DATA}_{ij} \right)^2}{2\sigma_j^2} \right] \prod_i \frac{1}{\sigma_\alpha} \exp\left[\frac{-(\alpha_i - 1)^2}{2\sigma_\alpha^2} \right] \prod_j \exp\left[-\frac{s_j^2}{2\sigma_j^2} \right] \qquad \text{(S20)}$$

Here, i is an index over lanes, and j is an index over residues. The parameters are as follows: α_i are the lane normalization parameters; σ_a is the lane loading error; C_j^{unfold} is the cleavage intensity of the unfolded state; ΔC_j is the change in cleavage intensity between the unfolded and folded states; σ_j are the errors associated with each residue; and s_j are the minimum errors assigned to each residue (set equal to 0.1 times the mean of DATA_{ij} across all lanes).

This model has been implemented in MATLAB. Given a prediction for the folding isotherm f_{fold}, maximum likelihood estimates for C_j^{unfold}, ΔC_j, α_i, σ_j, and s_a are determined by iteration. It is first assumed that $a_i = 0$, s_j = constant, and the maximum likelihood cleavage patterns of the unfolded and folded states are estimated. With these initial estimates, the s_j are updated, then the a_i, then the s_a; and the procedure is iterated five times (empirically, after three iterations, the procedure appears to converge within 0.1 log likelihood units).

For the full likelihood analysis, a range of K_1 and K_2 were explored, varying both parameters from 10^{-2} mM to 10^2 mM and computing the likelihood in equation S20. Contours of these likelihood fits are given in Figure S3; it is apparent that for each construct, a wide range of K_1 and K_2 are consistent with the data, though the two parameters are strongly correlated. In particular, for low K_1, a range of models with $(K_2)^2/K_1$ = *constant* gives similar predictions for the fraction folded (equation S8) with similar likelihoods.

Comparing likelihoods of thermodynamic models across different gels

One of the advantages of likelihood analysis is that replicates are not formally necessary to estimate errors like the σ_j of equation S20; these errors, and the corresponding likelihoods, are effectively read out for each gel from the intrinsic scatter of the data. Nevertheless, it is still important to compare the likelihood analyses made with independent gels for consistency. Figure S3 shows likelihood contours (with log-likelihood within 2 of the maximum likelihood, corresponding to approximately ~95% confidence) for the experiments presented in the main text, with replicates shown as differently colored contours. Replicates for each construct with each metal ion are in excellent agreement; their data can be combined (by multiplying likelihoods from replicates) with confidence and lead to tighter likelihood contours (black contours in Figure S3).

Estimating rescue factors

For the ΔG to be well-defined in Model 1 with respect to $[M^{2+}]$, the variation in free energy of the unfolded state needs to be the same across different constructs (but can be different for Mn^{2+} versus Mg^{2+}), and thus K_1 is a constant across constructs. The posterior distributions for the relevant K_1 parameter for the different constructs are given in Figure S7. These posterior distributions are obtained by integrating the likelihood estimates over $\ln(K_2)$. The distributions do not strongly constrain K_1 and are consistent with each other. Our best estimate for K_1 is given by the product of the posterior probabilities for the different constructs (black curve in Figure S4).

The posterior distributions of K_2 are similarly broad. However, to estimate $\Delta\Delta G$, we are interested in the *ratios* of K_2 (equation S12b) between the unmodified constructs and each phosphorothioate construct, which are better defined. Carrying out the integrations over $K_1(Mn^{2+})$ and over $K_1(Mg^{2+})$, and convolving the posterior probability distributions for $\Delta\Delta G$, gives the final distributions shown on the right hand side of Figure S5. We note that the final distributions are symmetric and indistinguishable from Gaussian curves, although this was not assumed in the analysis. Indeed, the underlying likelihood contours [Figures S3 and S5 (left)] are strikingly non-Gaussian.

Tables of the 95% confidence intervals for free energy values in equation S22 are given in Table S3. It is apparent that only the A184 R_P, A184 S_P, and A184 PS_2 constructs are consistent with metal ion rescue effects. The experiments for G188 R_P and G163 R_P do not give evidence for significant rescue. The data and their errors are in excellent agreement with Table 1 in the main text, which used simpler fits.

A fully analogous likelihood-based analysis was carried out to implement fits to Model 2 (linear expansion of the apparent Hill coefficient). Again, the resulting values and confidence

intervals (Table S4) are indistinguishable within error from the simpler fits in Table 4 in the main text.

SUPPLEMENTAL MATERIAL FIGURE LEGENDS

Figure S1: Strategies for constructing ΔC209 P4-P6 RNAs with site-specific phosphorothioate substitutions. We used HPLC to separate synthetic phosphorothioate oligonucleotide diastereomers (Hougland et al. 2005; Frederiksen and Piccirilli 2009) and incorporated them into full-length ΔC209 P4-P6 RNAs via successive splinted enzymatic ligations (Moore and Sharp 1992; Silverman and Cech 1999). **(A)** Splint ligation schemes for RNA construction. **(B)** Schematic of phosphorothioate linkages used in this work. **(C)** Typical anion exchange HPLC trace showing the separation between R_P and S_P single-phosphorothioate diastereomers.

Figure S2: A model using a constant Hill coefficient does not adequately fit the footprinting data. The plots show Mg^{2+}- and Mn^{2+}-dependent (open versus closed symbols) folding of unmodified ΔC209 P4-P6 (top) and the A184 S_P phosphorothioate variant in a background of 2 M NaCl. The data are fit to a Hill equation in which n_{Hill} either varies (solid lines) or is set equal to 2 (dashed lines).

Figure S3: Likelihood analyses from independent gels give consistent results. For each construct and metal ion, contours are shown marking values of K_1 and K_2 that have log-likelihood within 2 of the maximum likelihood point for different experiments. The black curve gives the analogous contour for the combined data, i.e., summing the likelihoods over the different experiments.

Figure S4: Posterior distributions over ln K_1 (the equilibrium constant for binding the "hidden" metal ion) do not exhibit a strong preference for particular values, and are consistent among different constructs. Black curves give final posterior distributions for $K_1(Mg^{2+})$ and $K_1(Mn^{2+})$

assuming that these values are the same across all constructs (obtained by multiplying posterior distributions for all constructs).

Figure S5: Estimating rescue factors for the different constructs. Left panels show log-likelihood contours (within 10 of maximum likelihood point) for the construct in Mn^{2+} (blue) and Mg^{2+} (red); and for unmodified ΔC209 in Mn^{2+} (light blue) and in Mg^{2+} (light red). Right panel shows posterior probability for rescue factor for K_2 (monitoring equilibrium constant between no metal ion and two metal ion state), after integration of the likelihood over ln K_1, and making the assumption that $K_1(Mg^{2+})$ and $K_1(Mn^{2+})$ are the same for all constructs, with distribution shown in Figure S4. Note that the rescue factor, when defined here in terms of ratios of K_2, is related to ΔΔΔG by eq. S12b.

Supplemental Figure S1

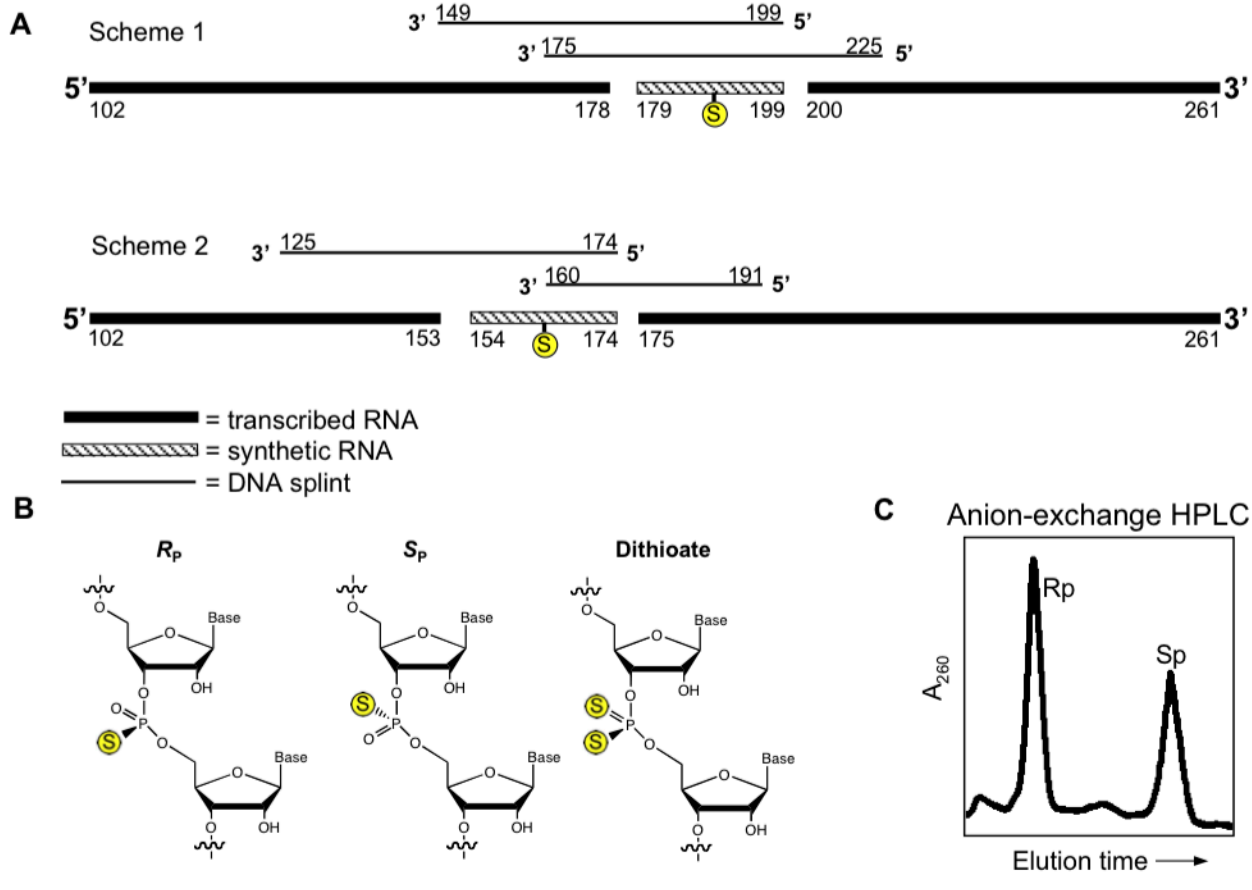

Supplemental Figure S2

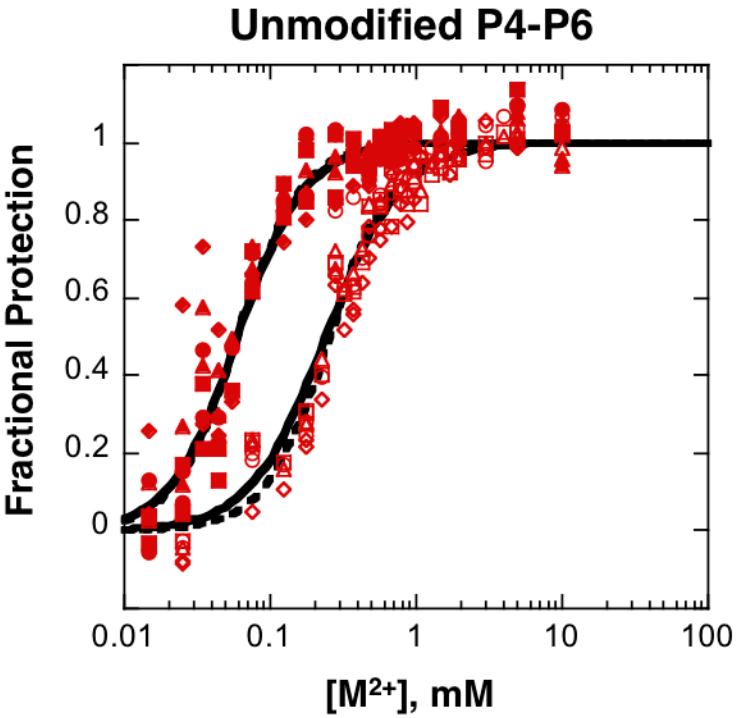

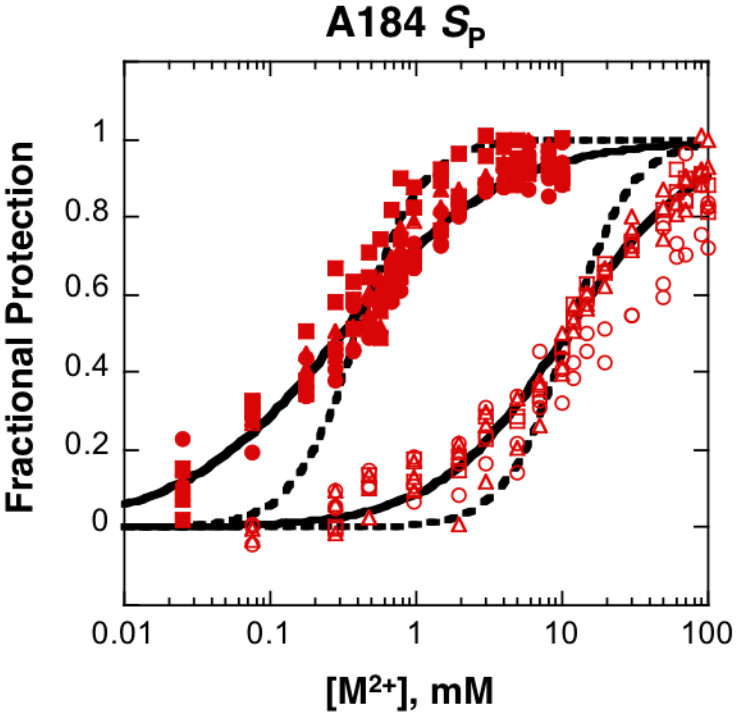

Supplemental Figure S3

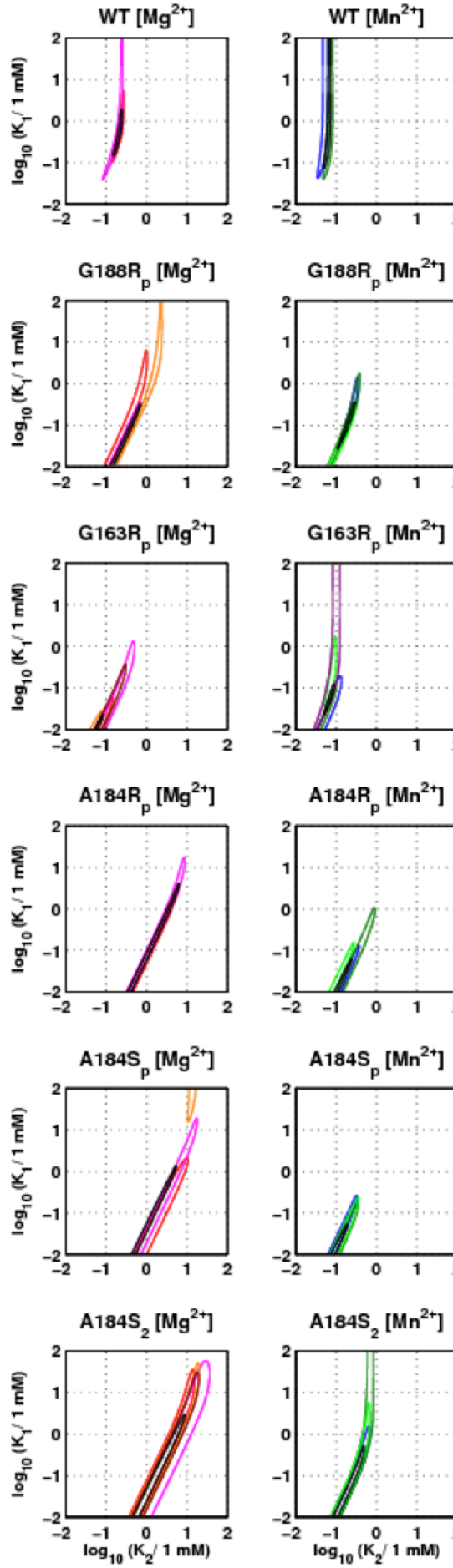

Supplemental Figure S4

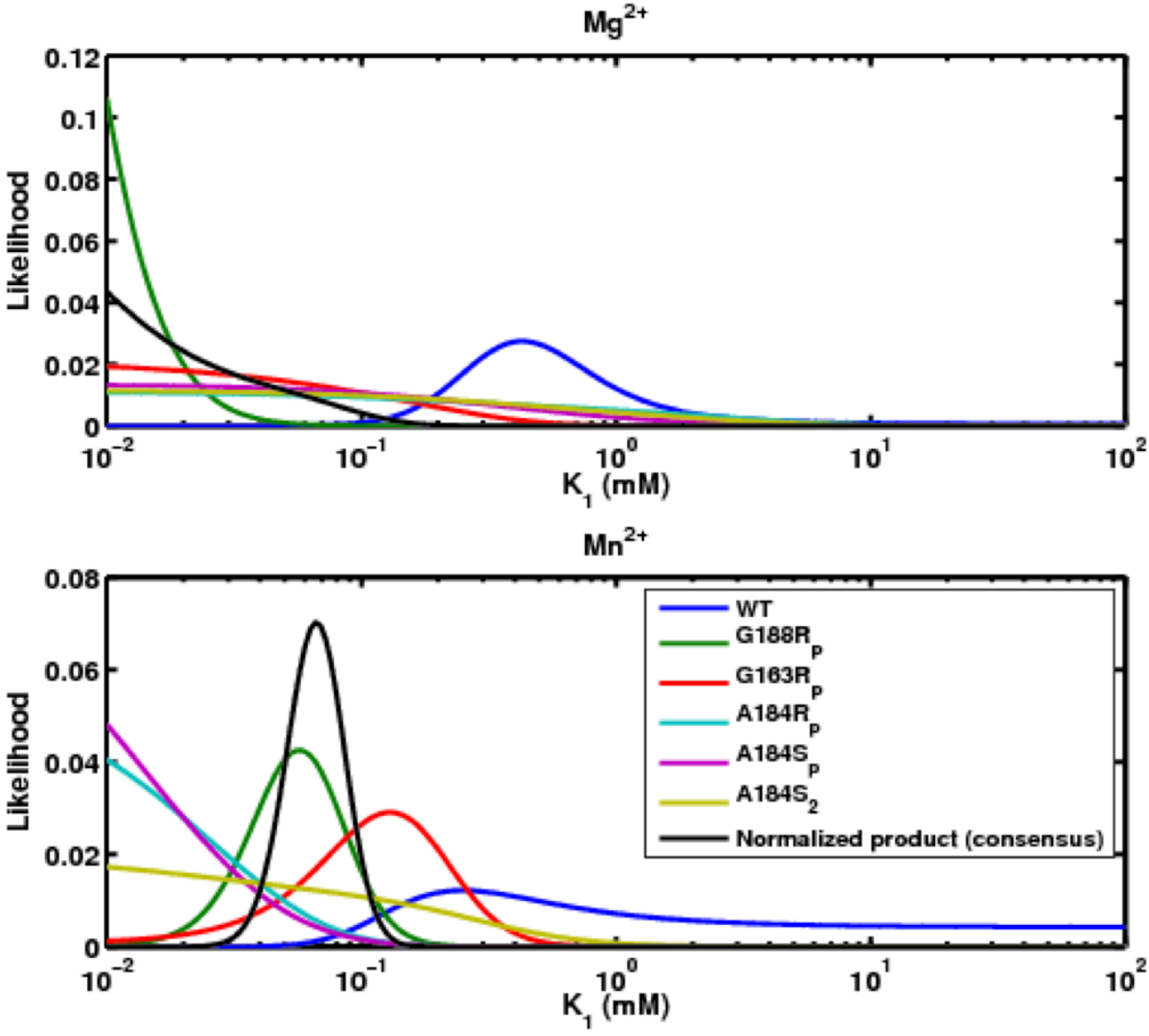

Supplemental Figure S5